Chemical Engineering Journal 479 (2024) 147923

Contents lists available at ScienceDirect

Chemical Engineering Journal

journal homepage: www.elsevier.com/locate/cej

Impact of H_2O on CO_2 adsorption and co-adsorption: Mechanism and high-performance adsorbents for efficient H_2O-CO_2 capture

Minghai Shen [a,b], Fulin Kong [a,b], Wei Guo [a,b], Zhongqi Zuo [a,b], Ting Gao [a,c], Sen Chen [d], Lige Tong [a,b,*], Peikun Zhang [a,b], Li Wang [a,b], Paul K. Chu [e,*], Yulong Ding [f,*]

[a] School of Energy and Environmental Engineering, University of Science and Technology Beijing, Beijing 100083, China
[b] Beijing Key Laboratory of Energy Saving and Emission Reduction for Metallurgical Industry, University of Science and Technology Beijing, Beijing 100083, China
[c] Experimental Center, School of Energy and Environmental Engineering, University of Science and Technology Beijing, Beijing 100083, China
[d] Basic Experimental Center of Natural Science, University of Science and Technology Beijing, Beijing 100083, China
[e] Department of Physics, Department of Materials Science and Engineering, and Department of Biomedical Engineering, City University of Hong Kong, Tat Chee Avenue, Kowloon, Hong Kong, China
[f] Birmingham Centre for Energy Storage & School of Chemical Engineering, University of Birmingham, B15 2TT, UK

ARTICLE INFO

Keywords:
Carbon dioxide
Water
Adsorption
Carbon capture
Direct air carbon capture

ABSTRACT

Physical adsorbents used for CO_2 capture from air directly and wet CO_2 flue gas have limited effectiveness due to competitive adsorption of H_2O and CO_2. Therefore, it is crucial to understand the impact of H_2O on CO_2 adsorption and investigate the co-adsorption mechanism in order to enhance the screening, design, and optimization of carbon capture systems. Herein, heat treatments are performed on commercial NaX zeolites to modify the composition of the O-T-O (T = Al, Si) framework. Our systematic investigation based on thermogravimetric analysis/differential scanning calorimetry (TG-DSC), infrared spectroscopy (IR), solid-state nuclear magnetic resonance (SSNMR), and density-functional theory (DFT) calculation, the connection between the structure of NaX zeolite and H_2O and CO_2 adsorption/desorption is established. The heat-induced changes in the O-T-O (T = Al, Si) framework produce movements of the loaded Na^+ ions. Hydrogen bonds formed by agglomerated adsorbed H_2O constitute the primary source of desorption heat, which adversely affects CO_2 mass transfer and adsorption. Our findings illustrate that modifying the distribution of Na^+ ions in the O-T-O (T = Al, Si) framework can reduce the CO_2 adsorption energy and prevent the formation of water agglomerates. Our findings provide insights into the design of efficient and high-capacity adsorbents for CO_2 capture that can be operated in the presence of H_2O.

1. Introduction

Since the concentration of CO_2 in the atmosphere is lower than that in industrial flue gases, traditional chemical carbon capture methods using alcohol amines, ammonia, and ionic solutions to capture CO_2 from ambient air may not be applied directly to flue gases. The potential environmental impact associated with the lifecycle of these methods including equipment, labor, operation, and maintenance costs often outweighs the benefits of capturing CO_2 from the atmosphere [1,2]. Despite recent advances in the reduction of the overall cost and energy requirements, these methods may not provide tangible benefits for enterprises and society [3]. Therefore, it is crucial to explore low-cost, high-efficiency direct air carbon capture technologies. However, the development of affordable, effective, energy-efficient, environmentally friendly, and safe CO_2 adsorbents for large-scale implementation is a daunting task [4].

The direct air carbon capture (DAC) process not only captures CO_2 selectively, but also adsorbs a significant amount of H_2O from air. Given the larger concentration of H_2O compared to CO_2 in ambient air, the co-adsorption of H_2O and CO_2 cannot be overlooked [5]. The presence of H_2O can either enhance or hinder the CO_2 capture capacity depending on the type of sorbents, and may even impact the long-term stability [6]. The influence of H_2O co-adsorption on amine-functionalized sorbents has been studied in recent years [7,8]. However, physical adsorption without amine groups offers a more straightforward approach than complex chemical adsorption processes and allows better control of the

* Corresponding authors at: School of Energy and Environmental Engineering, University of Science and Technology Beijing, Beijing 100083, China (L. Tong).
E-mail addresses: tonglige@me.ustb.edu.cn (L. Tong), paul.chu@cityu.edu.hk (P.K. Chu), Y.Ding@bham.ac.uk (Y. Ding).

https://doi.org/10.1016/j.cej.2023.147923
Received 29 September 2023; Received in revised form 29 November 2023; Accepted 4 December 2023
Available online 7 December 2023

adsorption selectivity. Madden et al. [9] have evaluated the CO_2 capture capacity of ten physisorbents and found that H_2O impedes adsorption, which can be mitigated by precise control of the pore size and pore chemistry.

In sorbent-based direct air capture (DAC) systems, in order to minimize the impact of H_2O on CO_2 capture, one approach is to incorporate an additional desiccant bed prior to the CO_2 adsorption bed for moisture removal [10]. However, this method presents certain challenges. Firstly, inclusion of extra desiccant beds increases the system complexity and cost and additional equipment and piping are required to facilitate desiccant circulation and regeneration. This not only escalates the equipment and operational expenses, but also increases the potential risk of system malfunctioning. Secondly, the desiccant bed requires additional space, potentially limiting the feasibility and adaptability of the system in practical applications. Furthermore, when selecting a desiccant and considering its regeneration process, other factors such as cost, sustainability, and environmental impact must be taken into account [11].

Co-capture reduces the amount of required adsorbent and device size, resulting in a smaller overall system volume and weight. This integration also facilitates easier regeneration of the adsorbent, enables multiple cycles, and improves the sustainability and economy of the adsorption process. The recovery of H_2O, an important resource in CO_2 utilization, daily life, and industrial applications, holds great significance and efficiency in the joint retrieval of CO_2 [12]. In the future, as DAC systems become more widespread, recovering H_2O from air can address operational challenges, particularly in regions with water scarcity such as deserts and arid coastal areas [13]. Additionally, advancements in photocatalysis, photothermal catalysis, and other technologies offer the opportunities to convert H_2O and CO_2 into high-quality fuels [14–16]. Therefore, future DAC systems require adsorbents that can achieve equilibrium adsorption while efficiently separating H_2O and CO_2.

Historically, DAC systems have predominantly utilized organic amine-loaded chemical adsorbents and alkaline solutions for CO_2 capture [17]. While these methods can effectively separate CO_2 from other impurities during adsorption, the reverse reaction during desorption and subsequent adsorbent/solution regeneration necessitate higher energy inputs (operating temperature >373.15 K). Porous materials utilized for physical adsorption of CO_2 rely on low-energy van der Waals forces and electrostatic forces [18]. In terms of environmental friendliness (amine-free) and low-energy/low-cost operation, physical adsorbents are highly desirable [19,20]. Among them, zeolites have gained considerable attention in gas separation due to their abundant porous structure, cost effectiveness, and well-established production processes [21]. Compared with other solid physical adsorbents (4A zeolite [22], ZSM-5 zeolite [23], metal-based MOFs [24], physical membrane [25], etc.), the large porous domain of NaX zeolite limits its adsorption selectivity for CO_2 and H_2O. While the adsorption selectivity of NaX zeolite for CO_2 and H_2O is limited due to its large pore size, its exceptional adsorption capacity and successful commercial implementation should not be overlooked. NaX zeolite delivers exceptional performance in purification systems for air separation while capturing more than 99.99 % of CO_2 and H_2O from air [26,27].

NaX zeolite, which is commercially mature and widely used in industry, is used as an adsorbent. On the one hand, it has high capacity, high adsorption selectivity, high hydrothermal stability and regeneration. On the other hand, zeolites are widely present minerals on the earth, and the preparation of NaX zeolite is relatively easy. This reduces production costs and increases sustainability. Compared with other adsorbents used for CO_2 capture, the structure of zeolite can be controlled through a variety of methods, thereby changing its pore size and surface properties, making it more suitable for the carbon capture process under specific conditions. For direct air carbon capture with low CO_2 concentration, NaX zeolite is undoubtedly one of the most economical and practical adsorbents.

Water is frequently found in atmospheres containing carbon dioxide gas, including air and industrial emission sources such as flue gas, biogas and natural gas. As far as adsorption is concerned, a wide variety of carbon dioxide separation materials exhibit many different behaviors in the presence of water. Depending on the material, water may promote or hinder CO_2 adsorption, increase or decrease the rate of CO_2 absorption, or even affect the structural integrity of the adsorbent. Studying the competitive behavior of CO_2 and H_2O on adsorbent materials can help design more effective adsorbents and improve the efficiency of carbon capture.

Current research activities on zeolite capture of H_2O and CO_2 can be divided into two approaches. The first approach focuses on adjusting the hydrophobicity of zeolites specifically for CO_2 capture [28]. However, the hydrophobic layer on zeolites affects the kinetics rather than the thermodynamics of adsorption. Consequently, the equilibrium capacity for water adsorption does not change, but the time required to reach equilibrium is significantly longer. The second approach explores the water adsorption properties of zeolites for applications such as air drying and water capture in certain regions [29]. The inclusion of Al^{3+} into the zeolite framework creates polar sites in the zeolite structure to render them hydrophilic [30]. Therefore, the hydrophilic/hydrophobic properties of zeolites can be optimized by adjusting the Si/Al ratio in the structures and large Si/Al ratios result in stronger hydrophobic characteristics of zeolites. Furthermore, optimizing the hydrophilic/hydrophobic properties of zeolites can enhance gas adsorption [31]. Co-adsorption of CO_2 and H_2O is influenced by the interactions between CO_2 and H_2O binding sites and their respective characteristics. The effects of H_2O on CO_2 adsorption thus depend on these factors. A better understanding of the impact of H_2O on CO_2 adsorption can assist researchers in analyzing the influence moisture when designing and selecting adsorbent materials. Moreover, by better understanding the co-adsorption mechanisms, researchers can optimize the chemical and physical properties of materials to enhance the adsorption capacity and selectivity of CO_2 and moisture.

Herein, the influence of H_2O on CO_2 adsorption and co-adsorption mechanism of commercially available NaX zeolites are investigated (Fig. 1, Table S1 and Fig. S1–2). CO_2 and H_2O exhibit similar adsorption behavior including shared or similar adsorption sites. During co-adsorption of H_2O and CO_2, the faster mass transfer of H_2O leads to preferential occupation of the co-adsorption sites. Additionally, agglomeration of H_2O molecules impedes diffusion and adsorption of CO_2. A systematic investigation on the temperature-induced structural changes of zeolites and their impact on adsorption of H_2O and CO_2 is performed. As Na^+ ions are commonly found at adsorption sites, their migration in the zeolite framework and subsequent redistribution influence the adsorption characteristics for H_2O. Our results also reveal that alteration of the zeolite framework affects the adsorption energy of CO_2 revealing a close relationship between structural changes and CO_2 adsorption.

2. Methodology

2.1. Material and characterization

The commercial NaX zeolites were purchased from Jianlong Micro-Nano New Materials Co., Ltd., Luoyang, China (Table S1). In the heat treatment, the commercial NaX zeolite was sintered in a muffle furnace at different temperatures (433.15, 523.15, 573.15, 623.15, 673.15, 723.15, 773.15 and 823.15 K) for 4 h. X-ray diffraction was performed on the Bruker D8 Advance with Cu K_α radiation ($\lambda = 1.540598$ Å), a step size of 2°/min, and a range of 5–90°. The structure was examined by field-emission scanning electron microscopy (ZEISS), and the specific surface, pore volume, pore diameter, and free energy were determined using a fully automatic specific surface and porosity analyzer (Autosorb-IQ-MP, Quanta, USA) in a high-purity nitrogen environment at 77 K. The sample was degassed at a temperature of 393.15 K in vacuum for 12 h

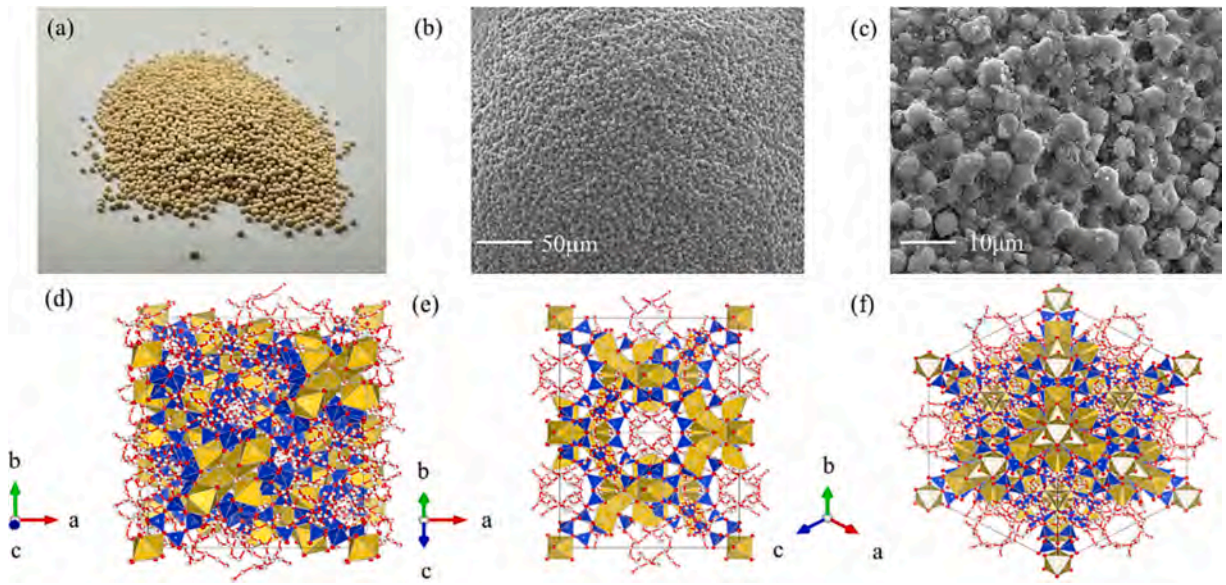

Fig. 1. NaX zeolite structure with different scales: (a) Macro appearance and see supporting information for details; (b–c) Surface morphology of the sample prepared by grinding the spherical particles in NaX zeolite which is octahedral with a rough surface and the binder used in molding making the surface uneven; (d–f) 3D NaX crystal structure at different angles.

before acquiring the adsorption isotherms and adsorption/desorption curves for CO_2 under high-purity carbon dioxide at 298 K.

The PQ001 nuclear magnetic resonance analyzer produced by Shanghai Numei Electronic Technology Co., Ltd. was used to determine the 2T characteristics of the transverse relaxation time. The magnetic strength, magnet temperature, and coil diameter were 0.55T, 32 °C, and 25 mm, respectively. There was a glass cylinder inside the coil and the sample was spread on the bottom of the glass cylinder. The transverse relaxation time 2T was measured by the CPMG pulse sequence. The NMR 2T relaxation spectra were obtained after inversion of the acquired signal by the inversion software MultiExp Inv Analysis that came with the instrument.

The infrared spectra were acquired from the zeolite on the Perkin Elmer Spectrum3 Fourier transform infrared spectrometer (FTIR). Potassium bromide compression was adopted and the scanning range was 4000 to 400 cm^{-1}. The XPS spectra were obtained on the Thermo Fisher Scientific ESCALAB 250Xi using a monochromatic Al K_α source with an energy of 1487.20 eV. The ^1H solid-state nuclear magnetic spectra were acquired on the Bruker Advance III HD at 400 MHz and the sample was first adsorbed and saturated in the N_2 containing water vapor.

2.2. Analysis of gas adsorption/desorption

The temperature-programmed adsorption/desorption behavior was analyzed by thermogravimetric analysis on the Setline Instrument (Fig. S3). The temperature of the sample was programmed from room temperature (293.15 K) to 453.15 K at a ramping rate of 10 K/min under flowing nitrogen (40 mL/min) and then cooled to 313.15 K after holding the temperature for 60 min to achieve complete desorption from the sample. Different gas flows were applied and the adsorption capacity for CO_2 was in 400 ppm CO_2/N_2 at a flow rate of 40 mL/min. The adsorption capacity for $CO_2 + H_2O$ (feedback in mass form) was determined in 400 ppm CO_2/N_2 + water vapor (controlling the water bath temperature to obtain a relative humidity of 40 % RH) at a flow rate of 40 mL/min. The desorption behavior including the concentration change of CO_2 and H_2O was analyzed by a flue gas analyzer (Shenzhen Watersell Co., Ltd.). The desorption exotherms were analyzed by differential scanning calorimetry on the Setline instrument. Different heating rates were used to study the form (physical or chemical bond) of the adsorbate in the adsorbent and the order of desorption.

2.3. Density-functional theory calculations

The unit cell unit of NaX was constructed based on the information in the literature. The lattice constant of 1 cubic NaX was 25.03 Å and the unit cell of NaX consisted of 556 O, 104 Si, 88 Al, and 41 Na atoms. NaX is described in the supporting information. Based on these initial structures, Castep's geometric optimization was performed to derive the most stable configuration of NaX and then the optimized structures were used in the simulations. During optimization, the atom positions and shape of the unit cells are not fixed. Since the unit cell of each NaX phase was large, only the smallest repeating unit was optimized and the Gamma point was sampled. The unique localized functional CA-PZ and local density approximation (LDA) methods were used to correct the unit cell structure. The membrane potential was Ultrasoft (ultrasoft), and the energy cutoff (cutoff energy) was 450 eV [32].

Molecular dynamics simulations were carried out using the Forcite program in Materials Studio 8.0, and the force field parameters were taken from the literature. NPT (combined isothermal-isobaric) simulations were performed at 0.0 GPa and 50, 100, 200, 300, 433.15, 523.15, 573.15, 623.15, 673.15, 723.15, 773.15, and 823.15 K. The temperature and pressure were controlled by the Andersen thermostat and Parrinello barometer, respectively. The simulation time was 500 ps and the data collected in the last 200 ps were used to analyze the thermal expansion behavior.

The structural changes after the heat treatment were probed using Quench in the Forcite program and all parameters were the same as aforementioned. The number of iterations was 500, and the energy, force and displacement convergence were set to 1×10^{-4} Ha, 5×10^{-3} Ha and 5×10^{-5} Å, respectively. Among the obtained structural models at different temperatures, a model that was similar to the molecular dynamics simulation structure at the corresponding temperature was selected [33].

The adsorption behavior was simulated using the Sorption program in Materials Studio 8.0. The structural models obtained by heat treatment at different temperatures were subjected to the (1 1 1) cleaved surface. A vacuum layer of 10 Å was subsequently established. The adsorption isotherm and fixed pressure task were used on the cut surface, respectively, and CO_2 and H_2O passing the geometric optimization in Castep were adsorbed by the Metropolis method. The starting pressure was 0.001 kPa and the ending pressure was 0.01 and 0.1 kPa,

respectively.

3. Results and discussion

3.1. Adsorption mechanism of CO_2 and H_2O of NaX

By analyzing the Differential Scanning Calorimetry (DSC) spectrum, information about the thermal properties of the sample can be obtained, such as melting point, crystallization temperature, reaction heat, glass transition, etc. [34,35]. DSC is widely used in materials science, drug research and development, food industry and other fields. DSC is performed to determine the physical properties of CO_2 and H_2O adsorption on NaX. Depending on the adsorption type (physical or chemical adsorption) of different adsorbates in the desorption process, the heat of desorption varies [36]. The heat peaks reflect the respective adsorption types of CO_2 and H_2O of NaX.

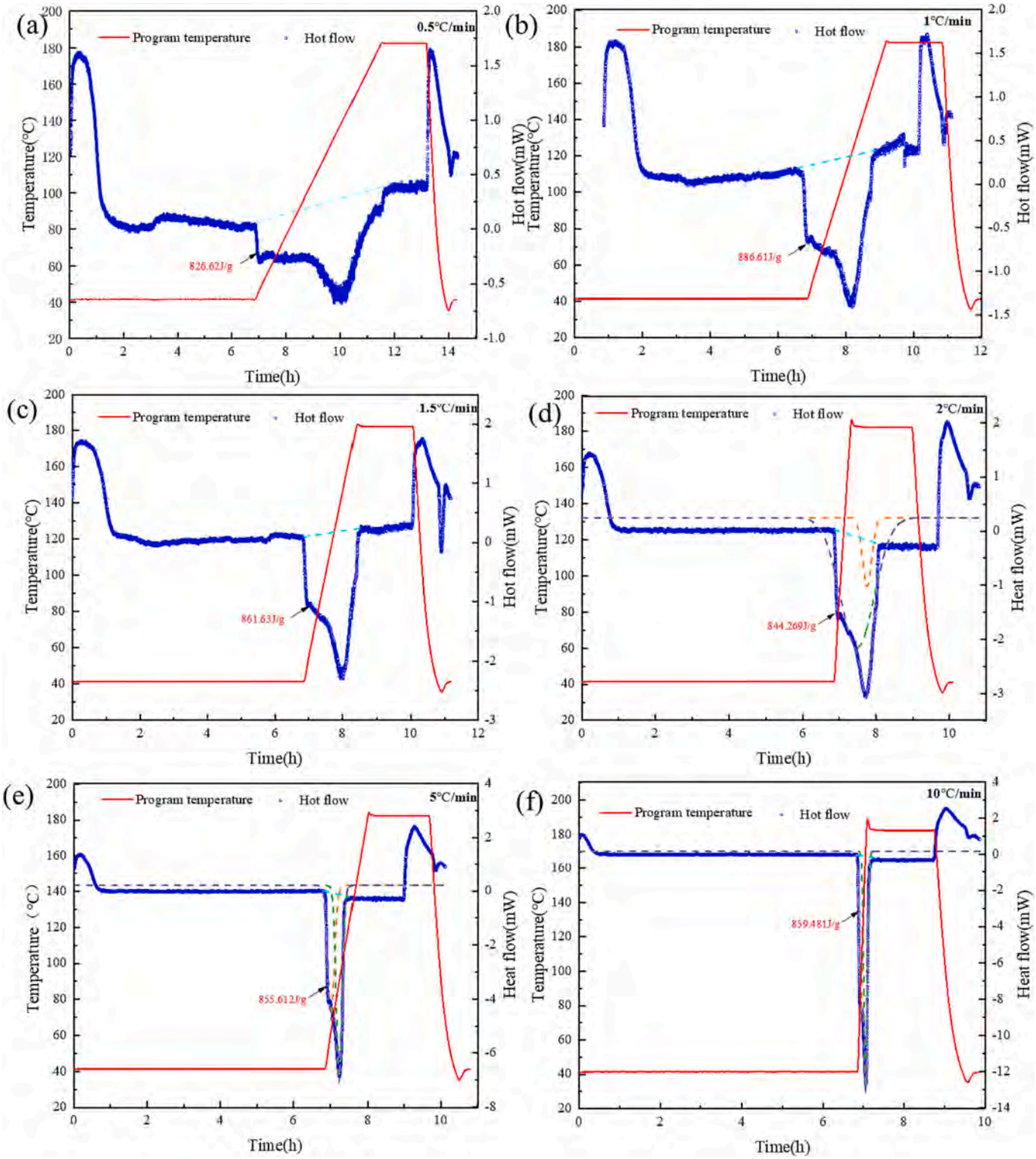

Fig. 2. Desorption of H_2O on NaX for different heating rates: (a) 0.5 ℃/min; (b) 1 ℃/min; (c) 1.5 ℃/min; (d) 2 ℃/min; (e) 5 ℃/min; (f) 10 ℃/min.

3.2. Adsorption of H_2O of NaX

First, NaX zeolite is selected for saturation adsorption by N_2 containing water vapor. using TG-DSC apparatus (TG mass stays unaltered). The desorption of H_2O is an endothermic process since the adsorbent's process of adsorbing H_2O is exothermic. As a result, using DSC technology at various heating rates, the endothermic peaks of H_2O adsorbed by NaX during the desorption process may be examined, as shown in Fig. 2a–f. Endothermic peaks usually rise, while exothermic peaks fall. The width of the thermal peak can also provide information about the reaction rate. The NaX desorption heat flow curves of H_2O at heating rates of 0.5 ℃/min, 1 ℃/min, 1.5 ℃/min, 2 ℃/min, 5 ℃/min and 10 ℃/min were obtained respectively. It can be found that as the heating rate increases, the time for NaX to desorb H_2O decreases. When the heating rate is higher, the instantaneous high thermal energy can perform multiple types of H_2O desorption simultaneously. When the heating rate is lower than 2 °C/min, the peak shape and peak valley of the heat flow peak can be observed more clearly. According to the fitting results, two obvious heat flow peaks appear when H_2O adsorbed in NaX is desorbed.

By integrating the area under the thermal peak, the total amount of heat absorbed during the desorption process can be obtained. Fig. 2 shows the desorption heat value of the same mass of NaX after saturated H_2O adsorption, with an average value of 855.70 J/g. Since thetotal heat of desorption is basically the same, the change in the heating rate can change the time of desorption heat for each type of adsorbed materials. Analysis of the peak time of the desorption peak is obvious. According to the control of the desorption heating rate, the adsorbent of two different adsorption forms can be separated. The separation principle is equivalent to the working principle of gas phase and liquid chromatography. The adsorption type is determined by the force of each adsorption form (physical or chemical adsorption, adsorption strength, etc.). The starting time and ending time of heat absorption are obtained by fitting the peaks of different types of adsorbed substances. The separation of desorption is realized by using the time difference between the start and end.

Due to the different distribution positions of adsorbed H_2O in the adsorbent, different NaX adsorption sites have different adsorption energies for H_2O. Exploring the adsorption form of H_2O in NaX will help us analyze the distribution of H_2O adsorption sites and the adsorption energy of H_2O at different sites. Low Field-Nuclear Magnetic Resonance (LF-NMR) is mainly used in the study of physical properties, using relaxation time and diffusion coefficient parameters to reflect the dynamic information of molecules in the sample. The strength and size of the 1H signal in water is an important basis for effectively determining the distribution and binding form of water. To analyze the form of H_2O in NaX, the transverse relaxation time is determined by low-frequency NMR. The magnitude of the transverse relaxation time represents the strength of the binding energy of water in the zeolite, and the smaller the transverse relaxation time, the stronger the binding energy with water [37]. Different peaks represent different bound forms of moisture. The peaks with relaxation times between 1 and 10 ms indicate the presence of weakly chemically bound water and those in the range of 10–100 ms indicate physically bound water. The pristine sample shows weakly chemically bound water (2.8–3.4 ms), indicating that the weakly chemically bound Na^+ formed with water is by adsorption (Fig. S4). This means that it has a relatively strong weak chemical adsorption energy compared to other samples, and desorption consumes more energy.

3.3. Co-adsorption of CO_2 and H_2O of NaX

In order to further analyze the adsorption/desorption mechanism of CO_2 and H_2O in NaX when CO_2 and H_2O are co-captured. After determining the adsorption form of H_2O in NaX for preferential diffusion mass transfer, the desorption heat flow after NaX adsorbed CO_2 and CO_2-H_2O respectively after saturation was also obtained based on DSC technology. There are 3 heat flow peaks and 6 heat flow peaks in the desorption process of CO_2 and CO_2-H_2O on NaX, respectively (Fig. 3a,b). During co-adsorption of CO_2 and H_2O on NaX, free H_2O in the form of hydrogen bonds accounts for the largest composition (peak 4). The weak physical adsorption of CO_2 with H_2O and O-Si-O is the weakest force in NaX (peak 1 and peak 2). Therefore, CO_2 first absorbs heat and desorbs in peak 1 and with the appearance of peak 2, some of the adsorbed H_2O desorbs (peak 3). Free H_2O (peak 4) continues to absorb heat for desorption. With the continuous supply of heat, the weak chemical adsorption of H_2O with Na^+, CO_2 and O-Al-O begins to break (peaks 5 and 6). As shown in Fig. 3c–e, based on the intermolecular force and adsorption capacity, the analysis of CO_2 and H_2O in NaX is described in the following (the peak number shows the order in which the force breaks):

(1) When NaX only adsorbs H_2O, Na^+ forms weak chemical adsorption with OH– in H_2O, and H^+ in H_2O also forms weak chemical adsorption with the acidic skeleton O-Al-O. Adsorption also occurs due to the hydrogen bonds between H_2O and H_2O (binding energy − 5.72 kcal/mol, Table S2). Therefore, as adsorption proceeds, there will be a stream of physically adsorbed water in the form of "agglomeration" in NaX. When NaX only adsorbs CO_2, since Na^+ and O-T-O (T = Al, Si) form a balanced electric field, CO_2 adsorbs near them by van der Waals force and electrostatic force forming weak physical adsorption. Since there is no active adsorption between CO_2 and CO_2 (binding energy 0.14 kcal/mol), in the same skeleton, the adsorption capacity of H_2O is smaller than that of CO_2.

(2) When H_2O and CO_2 are adsorbed by NaX at the same time in a humid air environment, the concentration of CO_2 (400 ppm) is lower than that of water vapor in air (RH 40 %). At a low partial pressure, H_2O has lower adsorption energy in NaX, and the mass transfer rate of H_2O is higher than that of CO_2 (Figs. S5a–d). Therefore, H_2O reaches the adsorption site first preempting the lower adsorption energy. With the formation of "agglomerated water", there is "dissolved" Na^+ [38] but on the other hand, a wall is formed to prevent diffusion of CO_2 and shield the force of internal adsorption sites on CO_2. Therefore, when H_2O and CO_2 adsorb together, the adsorption capacity of CO_2 is much lower than that of H_2O.

It is believed that the presence of H_2O accelerates CO_2 adsorption to saturation [39,40]. However, the mass transfer resistance and shielding effect render the remaining internal O-Si-O sites unable to adsorb CO_2. Since H_2O reacts reversibly with CO_2 to form unstable H_2CO_3, slight adsorption will also occur between H_2O and CO_2 molecules (binding energy −2.10 kcal/mol) and therefore, a small amount of CO_2 adsorbs onto the outer end of the H_2O chain.

3.4. Effects of the NaX skeleton change on CO_2 and H_2O adsorption

After observing the adsorption forms of CO_2 and H_2O in NaX, how to regulate the adsorption of CO_2 and H_2O and inhibit the adsorption of H_2O is what we want to explore next. Compared with designing zeolites with different pore size types through complex synthesis techniques. We use a simpler temperature effect to change the pore size structure of the zeolite. By discussing the influence of different pore size structures produced by temperature effect on the adsorption of CO_2 and H_2O by NaX zeolite, the key factors affecting the competitive adsorption of CO_2 and H_2O are analyzed.

3.5. Molecular dynamics simulation of changes in the structure of NaX zeolite under temperature effect

Molecular dynamics (MD) simulation is used to analyze the effects of temperature on the cell parameters such as bond length and bond angle in the NaX zeolite crystal structure. In the range of 50–823.15 K, the unit

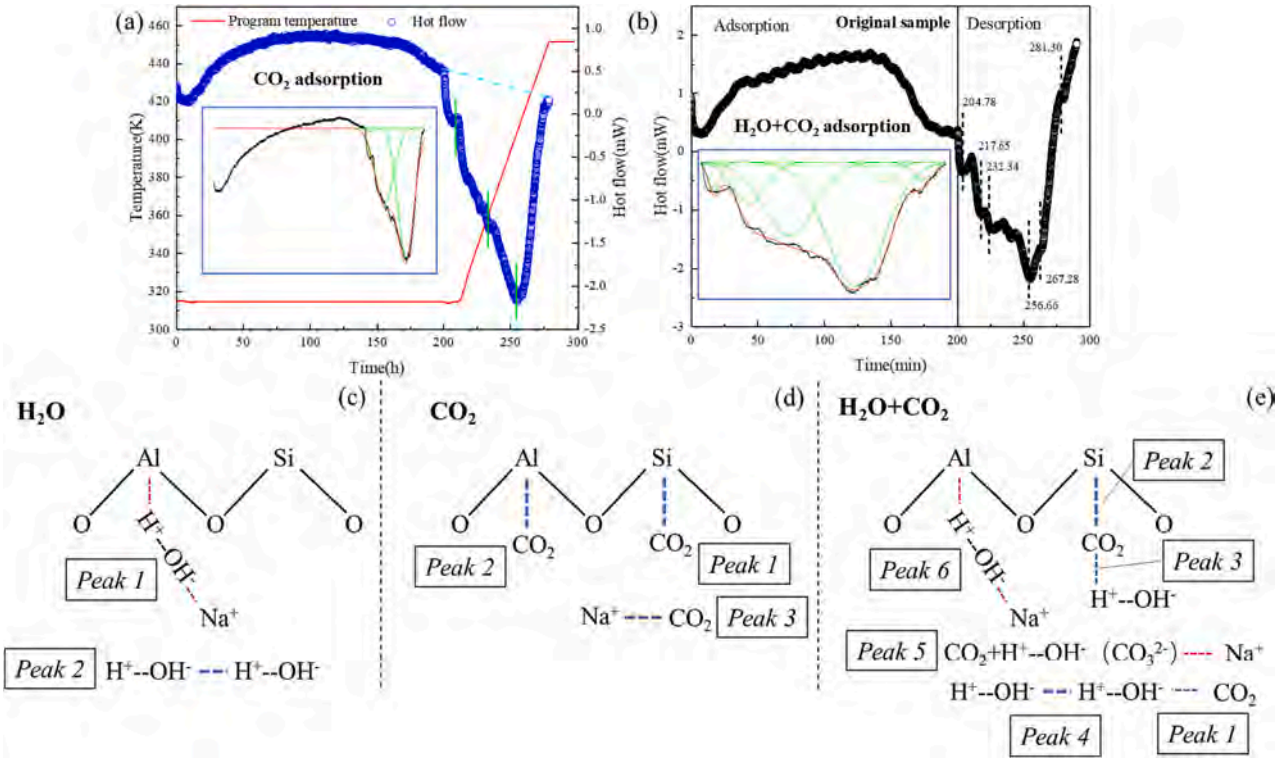

Fig. 3. Adsorption/desorption mechanism of CO_2 and H_2O in NaX derived by DSC: (a) CO_2 and (b) H_2O desorption heat flow and fitted peaks of NaX; (c–e) H_2O, CO_2, and CO_2-H_2O adsorption sites and desorption sequence in NaX.

cell type and lattice constant of NaX do not change in terms of the type and magnitude (Table S3). However, the angle and bond length between O-T-O (T = Al, Si) change (Table S4). In the range of 433.15–823.15 K, NaX exhibits positive thermal expansion (Fig. 4a,b). NaX shows insignificant negative thermal expansion in the range of 50–300 K as demonstrated previously [32].

Further analysis in the 433.15–823.15 K temperature range discloses that the NaX zeolite bond length and bond angle change. Due to the twelve-membered ring framework, the energy in this temperature range is not enough to break the ring framework, and there is no obvious collapse of the framework [41]. O-Al-O and O-Si-O will restrain each other, resulting in large shrinkage in the porous structure. The average bond length of Al_1-Al_1 does not change considerably in the temperature range of 50–433.15 K, but fluctuates from 433.15 to 823.15 K (Fig.S6a, b). The average bond length of Si_1-Si_1 is stable only between 50 and 100 K, but fluctuates as the temperature increases. Analysis of the angle change of O-T-O (T = Al, Si) reveals that the bond angle of O-Al-O is relatively stable in the temperature range of 50–773.15 K (Fig.S6c,d). The bond angle of O-Si-O changes greatly in the temperature ranges of 50–200 K and 433.15–673.15 K. The results show that O-Si-O is sensitive to temperature and will produce shrinkage vibrations influenced by temperature, thereby changing the average bond length of Si_1-Si_1.

Since Na^+ in NaX is not in the skeleton chain, its motion is inconsistent with that of Si and Al. Pure silicalite is not acidic. When

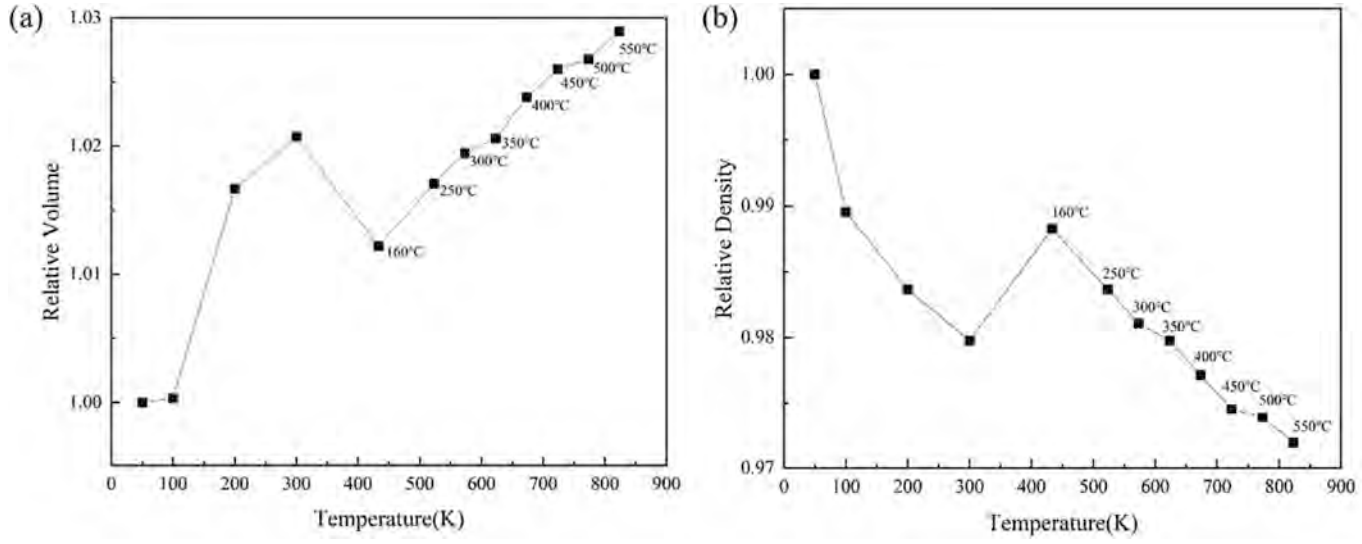

Fig. 4. (a)Relative volume variations of NaX at different temperatures simulated by MS; (b) NaX relative density change at different temperatures simulated by MS.

aluminum atoms are introduced into the zeolite framework to replace silicon atoms, Al is 3+ and Si is +4. Therefore, introduction of each framework aluminum atom generates one negative charge. In order to maintain electrical neutrality, the zeolite framework needs to absorb cations such as Na^+, K^+, Ca^{2+}, etc. to balance the charge [42]. Na^+ is reasonably distributed on the NaX twelve-membered ring with an electrostatic field (positive charge) and Lewis acids and bases (basicity). To maintain charge neutrality in the zeolitic materials, the Na^+ distribution indicates that the region forms an acidic field or negative charge density [43]. By monitoring the trajectory of Na^+, the acidity, alkalinity, and electric field change in the corresponding O-T-O (T = Al, Si) region can be analyzed. Water preferentially adsorbs at Na_3 sites [38]. The trajectory of Na_3 fluctuates greatly in the temperature range of 200–673.15 K but less so at other temperatures (Fig. 5a and b). In this temperature range, the acid-base and charge density fields inside the NaX zeolite show obvious changes. Since Al^{3+} is more basic than Si^{4+}, O-Al-O (AlO_4^+) is less acidic than O-Si-O (SiO_3^{2+}). Therefore, the movement of Na_3 is more obvious with changing O-Si-O bond angle (Fig.S6c and d; Table S5). The steric hindrance and interference of the O-T-O (T = Al, Si) charge field shift the Na_3 distribution angle up and down the O-T-O (T = Al, Si) plane (Fig. 5c and d).

Overall, the temperature effect changes the framework of NaX. Since the temperature change of 0–823.15 K is not enough to destroy the skeleton O-T-O (T = Al, Si) of NaX, O-T-O (T = Al, Si) will produce vibration contraction and stretching consequently affecting the acidity and alkalinity in the vicinity and causing migration of Na^+.

Most materials expand as temperature increases, but there are special materials that contract as temperature increases. Materials that shrink with increasing temperature exhibit negative thermal expansion. Zeolites are typical materials with a negative coefficient of thermal expansion [44]. Previous studies have demonstrated that the thermal behavior of zeolites is determined by the complex interactions between the zeolite framework and cations and water molecules in the channels [45–47]. Commercial zeolites are activated in dry air at low temperature (283.15–423.15 K) during production. This operation not only removes water from the zeolite (wetting water, adsorption water, and a part of crystallization water), but also improves the mechanical strength [48]. We compared the microstructural changes of NaX zeolite after sintering at 433.15–823.15 K. The temperature change does not affect the macrostructure of NaX zeolite (Figs. S7-9).

3.6. *Effect of NaX on CO_2 and H_2O adsorption performance under temperature effect*

In order to analyze the influence of temperature effect on adsorption performance, the adsorption performance of NaX zeolite sintered at different temperatures for CO_2, H_2O single adsorption and CO_2-H_2O co-adsorption is analyzed. As shown in Fig. 6(a), when CO_2 and H_2O are adsorbed alone, H_2O exhibits a better adsorption capacity. The original sample has the best adsorption capacity regardless of CO_2 adsorption

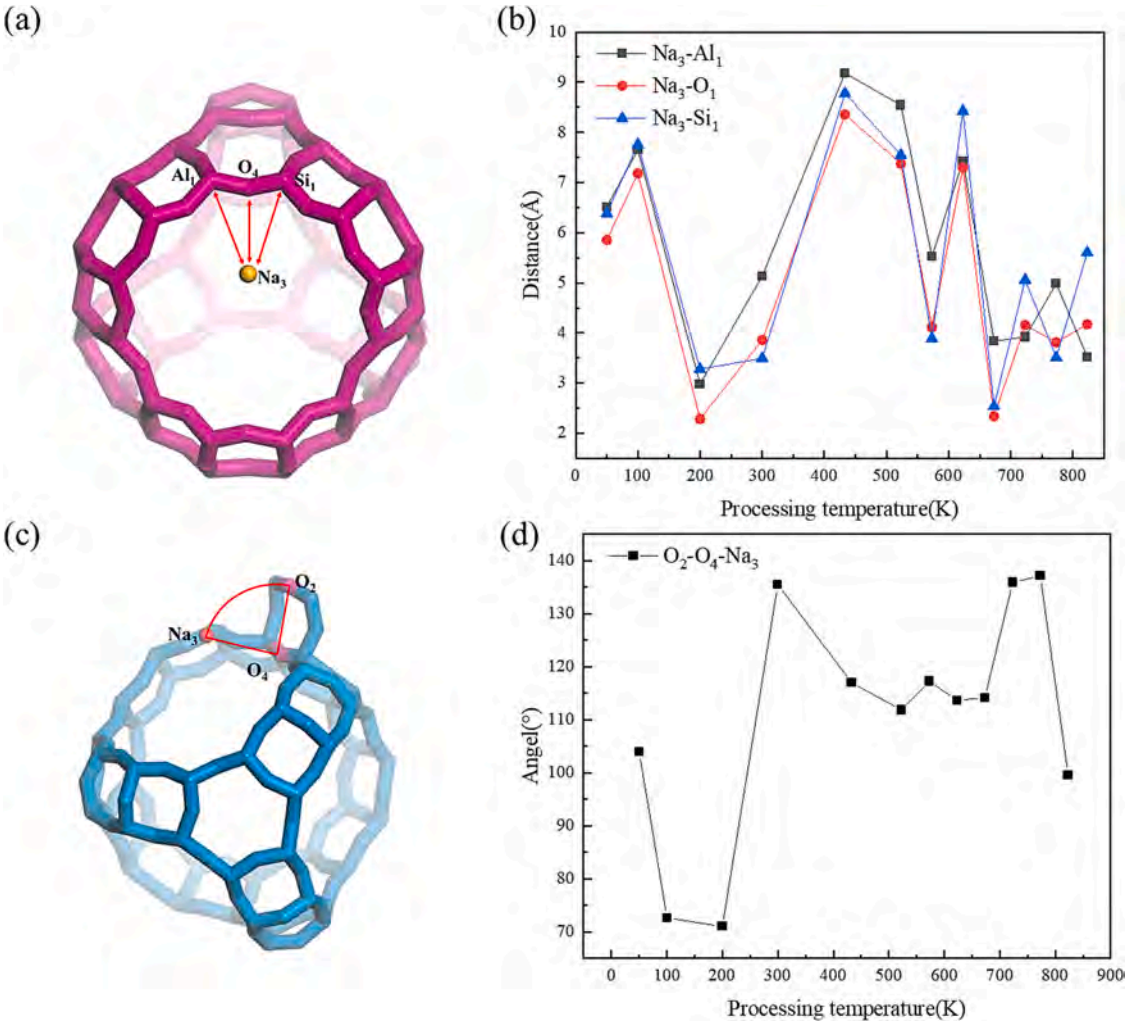

Fig. 5. Molecular dynamics simulation of the NaX skeleton changes at different treatment temperatures: (a) and (b) Distance change between Na_3 and Si_1, Al_1, O_1; (c and d) Migration track of Na_3 on the ring.

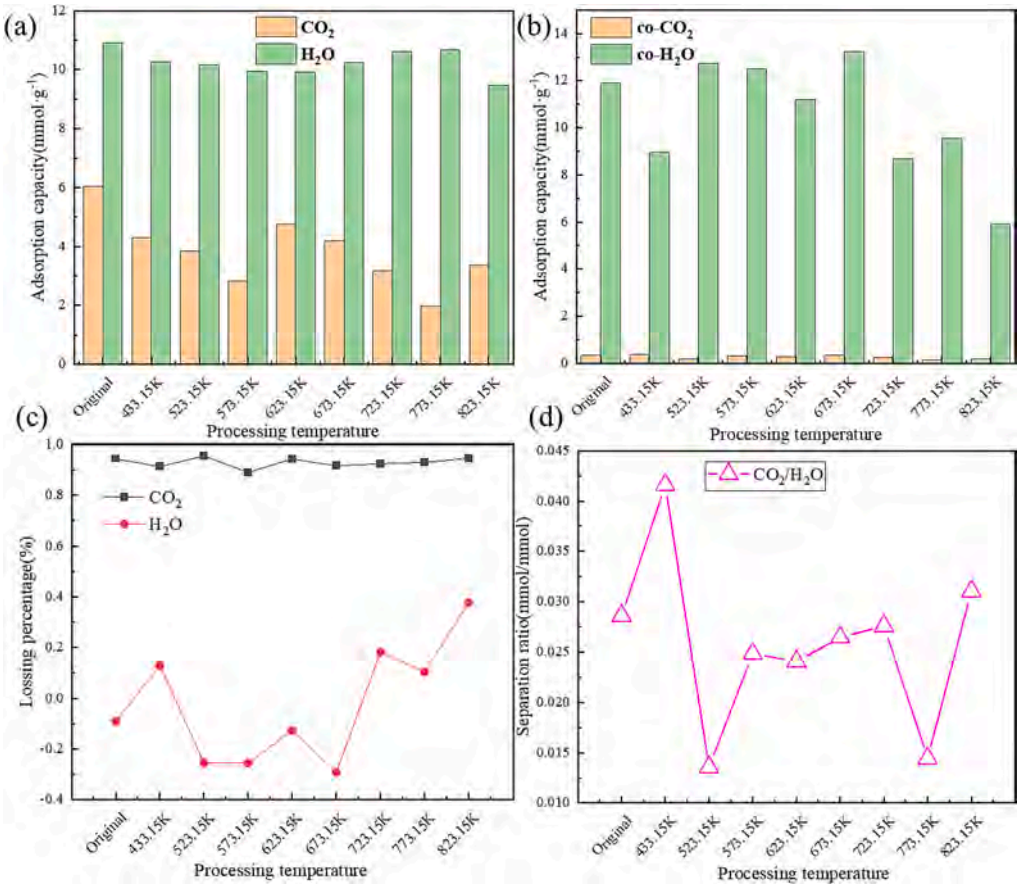

Fig. 6. Adsorption performance of NaX on CO_2 and H_2O at different treatment temperatures: (a) Adsorption capacity when CO_2 and H_2O are adsorbed separately; (b) Adsorption capacity when CO_2 and H_2O are co-adsorbed; (c) Loss of adsorption capacity when CO_2 and H_2O are co-adsorbed; (d) Separation ratios of CO_2 and H_2O during co-adsorption.

(6.05 mmol/g) or H_2O adsorption (10.90 mmol/g). As the treatment temperature increases, the specific surface area on NaX decreases and the overall adsorption capacity decreases (Table S6). The change in the NaX skeleton can modify the adsorption capacity of CO_2 and H_2O. For the sample at 773.15 K, the difference between the adsorption capacity of H_2O and that of CO_2 is the largest, reaching 8.69 mmol/g. Fig. 5(c,d) shows that for the sample at 773.15 K, Na_3 migrate to the inner part of the ring (O_2-O_4-Na_3: 137.11°). In the original sample, Na_3 is above the ring (O_2-O_4-Na_3: 54.791°). Considering that adsorption of CO_2 by NaX is mainly Na^+, as Na^+ migrates into the framework ring, adsorption of CO_2 is limited due to pore confinement and steric hindrance [49]. The adsorption energy of NaX to H_2O is lower and with the formation of "reunited water", Na^+ can dissolve and migrate and consequently, H_2O is less restricted.

When low-partial-pressure CO_2 and H_2O are adsorbed by NaX together, H_2O preempts a large number of CO_2 adsorption sites with faster mass transfer and lower adsorption energy. Therefore, the adsorption capacity of NaX for CO_2 during co-adsorption is lower than that of single adsorption, and the capacity decay is about 90 % as shown in Fig. 6(b,c). The change in the NaX skeleton has a certain influence on the adsorption capacity of CO_2 when CO_2 and H_2O are co-adsorbed, but it only increases by 9.4 mmol/g (433.15 K sample). Although the change in the NaX zeolite framework decreases the adsorption capacity of CO_2 during co-adsorption, it increases and decreases the adsorption capacity of H_2O during co-adsorption. The 673.15 K sample also reveals a higher adsorption capacity of NaX for H_2O during co-adsorption from 10.25 mmol/g when adsorbed alone to 13.23 mmol/g. This is due to the CO_2 in NaX, which can adsorb H_2O and be close to the hydrophobic O-Si-O framework, thereby increasing the distribution space of more H_2O. As the treatment temperature increases to 823.15 K, the adsorption capacity of NaX zeolite for co-adsorbed H_2O decreases by 37.74 % compared to single adsorption. The adsorption capacity of NaX for co-adsorbed H_2O decreases by 50.5 % in comparison with the pristine sample reaching 5.89 mmol/g. With increasing treatment temperature, NaX zeolite has a greater influence on the adsorption of H_2O when CO_2 and H_2O are co-adsorbed. This may be due to the sharp increase in the framework angle of O-Al-O, which reduces the force on the surrounding adsorbables [50]. The movement angle of Na^+ also drops. By modulating the O-T-O (T = Al, Si) structure, the surface energy can be reduced and by controlling the position of Na^+, the main adsorption sites of CO_2 and H_2O and adsorption capacities of CO_2 and H_2O are affected.

Considering that we want to recover CO_2 and H_2O simultaneously, the separation ratios are derived to evaluate the adsorption selectivity of NaX zeolite for CO_2 and H_2O, as shown in Fig. 6(d). The sample treated at 433.15 K shows a larger separation ratio from 0.028 (mmol/mmol) to 0.042 (mmol/mmol) indicative of the selectivity of NaX zeolite toward CO_2. The sample treated at 523.15 K exhibits a selectivity of NaX zeolite toward H_2O of 0.013 (mmol/mmol). Based on the temperature effect on the NaX zeolite framework, Na^+ moves to the farthest point of O-T-O (T = Al, Si) in the sample treated at 433.15 K.

3.7. *Effect mechanism of NaX structural change on CO_2 and H_2O adsorption*

The effects of temperature on the framework of NaX are assessed by infrared spectroscopy (IR). As shown in Fig. 7(a), as the treatment temperature increases, the characteristic peaks of the NaX framework gradually weaken [51,52], especially symmetric stretching. The peaks

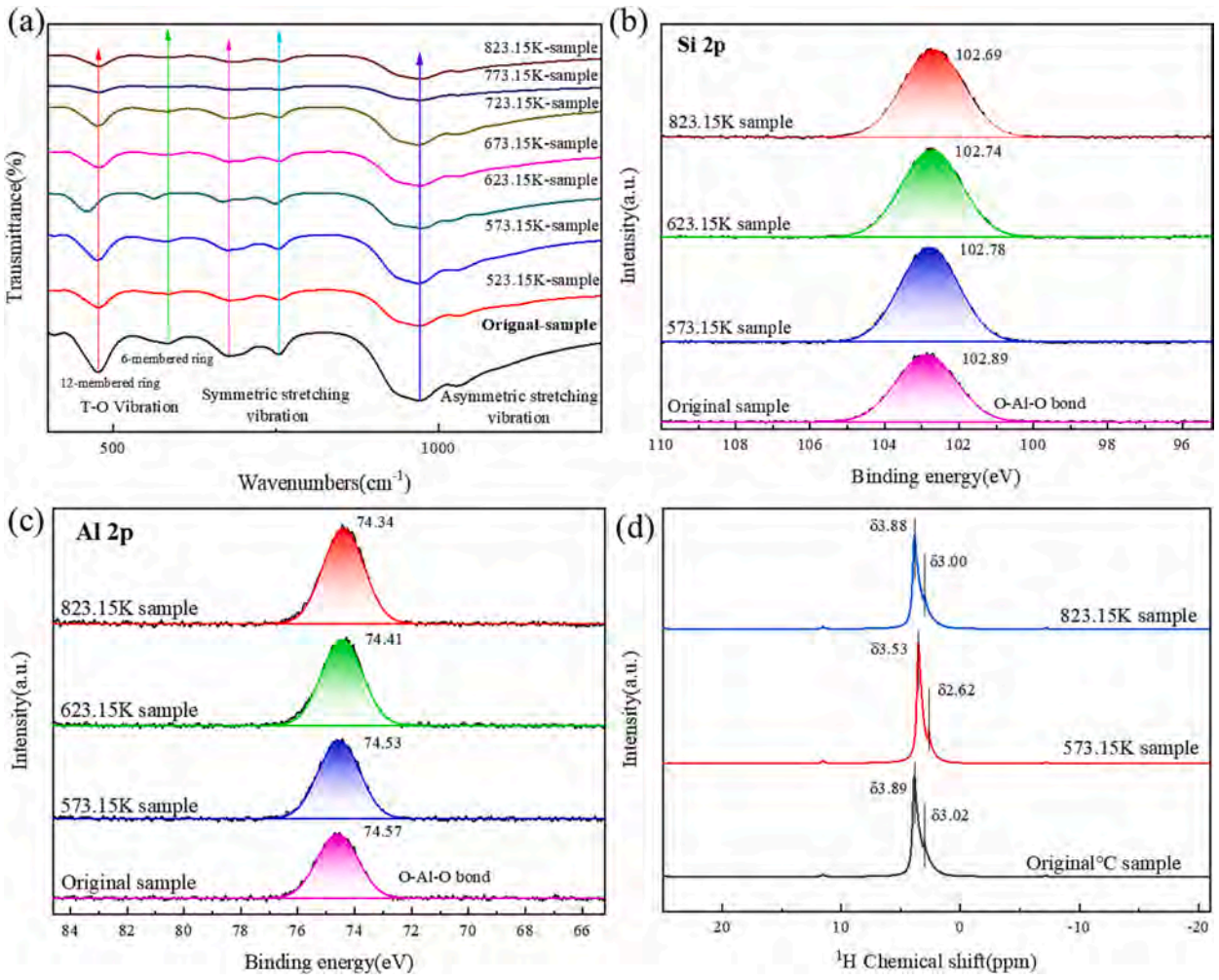

Fig. 7. Analysis of the skeleton change of NaX influenced by the temperature effects: (a) IR spectra of NaX; (b) XPS Si 2*p* spectra; (c) XPS Al 2*p* spectra; (d) ^{1}H MAS NMR spectra of NaX after adsorbing H_2O.

corresponding to asymmetric stretching and the twelve-membered ring framework still exist, indicating that the temperature effect does not break the framework of NaX. However, when the temperature is raised to 823.15 K, the asymmetric stretching peak and twelve-membered ring skeleton weaken. If the temperature goes up further, the framework of NaX breaks and collapses [45]. This is because the binding energy of O-T-O (T = Al, Si) decreases due to the temperature effect, as shown in Fig. 7(b,c) and Fig. S10a,b. The change in the bond length and bond angle of O-T-O (T = Al, Si) affects the electron cloud density in the vicinity consequently altering the acidity and negative charge of O-T-O (T = Al, Si).

Fig. S4 shows that the change of O-T-O (T = Al, Si) caused by the temperature effect alters the form of water adsorbed by the NaX zeolite. The samples treated at 433.15 K, 523.15 K, 623.1 5 K, and 723.15 K show small physical adsorption in addition to weak chemical adsorption. This indicates that the temperature-induced changes in the zeolite framework cause weak physical adsorption of water on zeolite O-T-O (T = Al, Si). Interestingly, the sample treated at 623.15 K has the smallest onset transverse relaxation time (2.0 ms) despite the presence of weakly chemically and physically adsorbed water. The adsorption process gives priority to chemisorption with a higher binding energy, and the desorption process takes priority to physical adsorption with a lower binding energy.

According to the high-frequency NMR ^{1}H spectra (Fig. 7d), the two ^{1}H peaks shift by different degrees similar to the migration of Na^{+}. The original sample and 823.15 K sample exhibit the similar ^{1}H peak and Na^{+} trajectory. However, the ^{1}H peak of the 573.15 K sample shows a large shift, which is consistent with the shift of the Na^{+} trajectory. Fig. S11-12 show that in the temperature range of 433.15 K-773.15 K, the position of each peak does not change by regulating the O-T-O (T = Al, Si) skeleton through the temperature effect. However, the peak areas of the CO_2 and H_2O desorption endothermic peaks are affected. This effect is mainly reflected by the desorption heat peak of adsorbed H_2O. Figs. S11(a) is consistent with Fig. 3(b), showing six main endothermic peaks. The peak around 270 min disappears as the treatment temperature is increased as shown in Fig. S11(b–h). When the temperature is higher than 823.15 K, the peak corresponding to agglomerated H_2O decreases significantly. The adsorption capacity of corresponding co-adsorbed H_2O also decreases significantly. The pore shrinkage and specific surface area decrease of NaX are the main reasons for the decrease in the free H_2O adsorption capacity. Fig. S12 shows that the structural change caused by the temperature effect affects the binding energy of CO_2 and H_2O adsorption. When CO_2 and H_2O are co-adsorbed, there is only one energy peak for CO_2 in Fig. S13, while as shown in Fig. S14 (a, c, d, f, g, h), there are multiple CO_2 adsorption energy peaks, and the peaks start shift to lower energies. These results indicate that the distribution and position of Na^{+} affect the adsorption performance of CO_2 and H_2O and by adjusting the zeolite framework, the migration trajectory of Na^{+} can be controlled. The EDS diagrams of NaX zeolite at different temperatures also prove the movement trajectory of Na^{+} (Fig. S15).

3.8. CO_2 and H_2O separation and recovery

Since the captured and separated CO_2 contains a large amount of desorbed water vapor, it usually needs to be dried and purified before being compressed and stored at a low temperature [53]. The freezing points of H_2O and CO_2 are quite different. In order to avoid blockage in the compressor and reduce the compression energy consumption, it is necessary to remove water vapor from CO_2 to above 99.99 % [54]. Condensers are used in air separation systems or industrial carbon capture, and external cold sources such as water cooling are used for heat exchange to separate water vapor from CO_2 [55,56]. However, increasing the separation rate of water vapor to above 0.9999 requires a high cooling capacity causing energy waste.

The energy consumption of 10 Nm^3/h of CO_2 streams with different water vapor contents separated by the condenser is calculated. The process flow is shown in Fig. S16, and the energy consumption calculation method refers to formula (1) in SI. After Aspen Plus process simulation, the steady-state operating condenser energy consumption can be obtained on the basis of ensuring component conservation, energy conservation, and compliance with actual operating operations. As shown in Table S7, as the purity of the target product CO_2 goes up from 99 % to 99.99 %, the cooling capacity or cooling water flow rate required to condense water vapor increases. When the water vapor content at the inlet increases, the energy consumption of water vapor separation also increases. For example, drying of 80 % water vapor requires 5 times as much cooling as 1 % water vapor. When NaX co-adsorbs CO_2 and H_2O, CO_2 adsorbs with less force and desorbs preferentially (Fig. 3d, Fig. S13b). Our previous studies show that there is a difference in the concentration peaks of CO_2 and H_2O in the gas stream after desorption [57]. For this reason, graded recovery can be realized based on the concentration difference of CO_2 and H_2O in the desorbed gas.

How to further realize the concentration difference graded recovery of CO_2 and H_2O, we combine the structural change rules of NaX zeolite under the temperature effect and give an outlook on future design based on material design. The design and adjustment of the zeolite structure can control the desorption starting time of CO_2 and H_2O. The pore confinement effect of zeolite can improve the stability of adsorbed molecules by van der Waals and electrostatic interactions, thereby changing the physical and chemical properties of the adsorbed species. In order to ensure the adsorption capacity of zeolite, controlling the range of binding energies can accomplish adsorption stability and low the energy consumption for desorption.

Fig. S14 shows that reducing the surface energy of the NaX zeolite by the temperature effect can reduce the adsorption energy of NaX for CO_2 and H_2O. Therefore, the energy required for desorption of CO_2 and H_2O that are weakly chemically/physically adsorbed changes. By controlling the temperature during desorption, the desorption rate of CO_2 and H_2O can be adjusted. Based on the priority desorption sequence of CO_2 in the desorption process, CO_2 with a small water vapor concentration is dried and recovered. As shown in Fig. 8(a,b), the desorption time of CO_2 is approximately 400 s, while the entire desorption process lasts about 1,700 s. This shows that in the 1/4 stage of the desorption process, CO_2 desorption is basically completed. According to the concentrations of the outlet CO_2 and H_2O, high-purity CO_2 (above 80 %) is dehydrated and recovered. However, low-purity (below 80 %) CO_2 carries water vapor, and desorption regeneration of the adsorption bed is carried out by the waste heat recovery technique [58]. When CO_2 desorption is completed, the remaining desorbed H_2O can be directly condensed and recovered with low energy consumption.

4. Conclusions

We report the adsorption mechanism of CO_2 and H_2O by NaX zeolite, one of the most commercially and industrially applied CO_2 adsorbents, and discuss its application value in direct air carbon capture. The competitive behavior of CO_2 and H_2O on adsorbent materials helps to design more effective adsorbents, improve the efficiency of carbon capture, and develop more efficient gas separation technologies. The following conclusions can be drawn:

(a) Due to the limitation of the O-T-O (T = Al, Si) framework, the temperature effect changes the structure of NaX irregularly. Reducing the surface binding energy of the framework affects the migration of Na^+ on the twelve rings. The temperature effect reduces the acidity and electron cloud density of the O-T-O (T = Al, Si) framework, resulting in less Na^+ being bound by the O-T-O (T = Al, Si) framework and migration.

(b) In the temperature range of 433.15–773.15 K, the adsorption capacity of H_2O during co-adsorption decreases as Na^+ migrates into the ring (the angle of O_2-O_4-Na_3 increases). The influence of NaX on H_2O adsorption during co-adsorption mainly depends on the distribution and position of Na^+. When the temperature is higher than 773.15 K, the pore size and specific surface of NaX decrease. Steric hindrance and pore confinement are the main reasons for the reduced capacity for H_2O in the form of agglomerated H_2O, which is mainly adsorbed by Na^+.

(c) During co-adsorption of CO_2 and H_2O, the weak mass transfer and high adsorption energy of CO_2 limit the distributions of

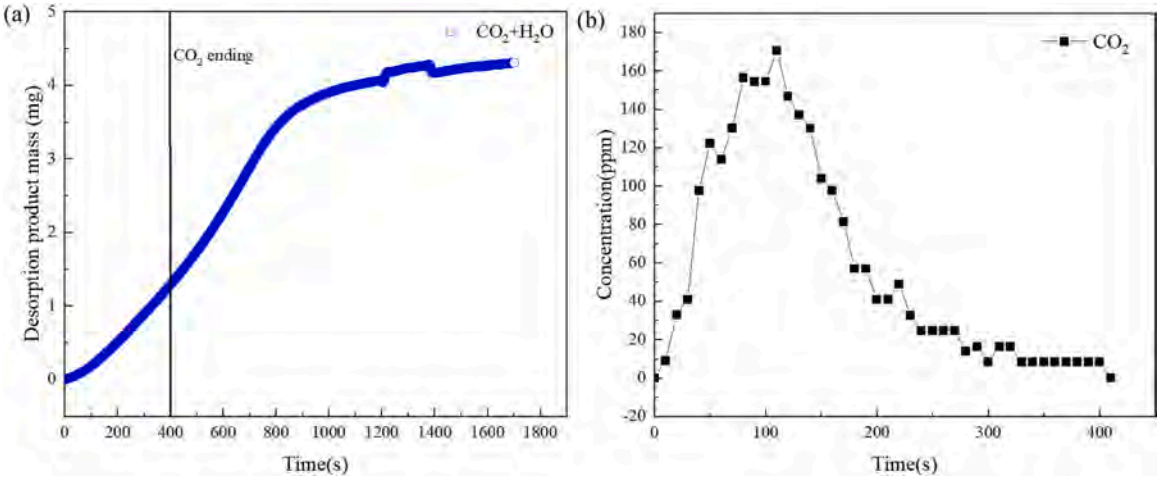

Fig. 8. Composition changes in the CO_2 and H_2O co-desorption process: (a) Mass change curve of CO_2 and H_2O during desorption and (b) Concentration change of CO_2 in the desorption tail gas.

adsorption sites. The change in the zeolite structure can reduce the adsorption energy of porous CO_2.

We believe that Na^+ sites can be fixed by rational design of the O-T-O (T = Al, Si) framework [59]. High-capacity co-adsorption of CO_2 and H_2O can be achieved by suppressing the adsorption of H_2O or separating the adsorption sites [60]. CO_2 adsorption on NaX is a physical phenomenon, and the presence of H_2O fixes a part of CO_2 with weak chemical adsorption. However, owing to the lower adsorption energy and more stable hydrogen bonds, H_2O occupies most of the adsorption sites for CO_2 thus having a shielding effect on the adsorption of CO_2. On the contrary, CO_2 preferentially desorbs during the desorption process. In the co-recovery process of CO_2 and H_2O, separation and recovery of high-purity CO_2 and H_2O can be achieved according to the desorption law of CO_2 and H_2O. Our results disclose that by proper design of the materials and separation technology, joint capture and recovery of CO_2 and H_2O by a direct air carbon capture system can be accomplished.

CRediT authorship contribution statement

Minghai Shen: Investigation, Methodology, Writing – original draft, Writing – review & editing. **Fulin Kong:** Data curation, Formal analysis, Writing – review & editing. **Wei Guo:** Methodology, Resources, Software. **Zhongqi Zuo:** Investigation, Resources, Software. **Ting Gao:** Methodology, Resources, Software. **Sen Chen:** Data curation, Methodology, Resources, Software. **Lige Tong:** Funding acquisition, Supervision, Writing – original draft, Writing – review & editing. **Peikun Zhang:** Methodology, Software, Validation, Visualization. **Li Wang:** Project administration, Validation, Writing – review & editing. **Paul K. Chu:** Project administration, Visualization, Writing – review & editing. **Yulong Ding:** Visualization, Writing – review & editing.

Declaration of competing interest

The authors declare that they have no known competing financial interests or personal relationships that could have appeared to influence the work reported in this paper.

Data availability

No data was used for the research described in the article.

Acknowledgements

This work was supported by the Beijing Natural Science Foundation (Grant No. 3232043) and City University of Hong Kong Donation Research Grants (DON-RMG 9229021 and 9220061). I would like to express my sincere gratitude to Pro Lu Qipeng for generously providing the software and granting the necessary permissions for its usage in this research. The availability of Materials Studio significantly contributed to the success of the experiments conducted in this study.

Appendix A. Supplementary data

Supplementary data to this article can be found online at https://doi.org/10.1016/j.cej.2023.147923.

References

[1] N. McQueen, K.V. Gomes, C. McCormick, K. Blumanthal, M. Pisciotta, J. Wilcox, A review of direct air capture (DAC): scaling up commercial technologies and innovating for the future, Progress in Energy 3 (3) (2021), 032001.
[2] M. Erans, E.S. Sanz-Pérez, D.P. Hanak, Z. Clulow, D.M. Reiner, G.A. Mutch, Direct air capture: process technology, techno-economic and socio-political challenges, Energy Environ. Sci. 15 (4) (2022) 1360–1405.
[3] G. Realmonte, L. Drouet, A. Gambhir, J. Glynn, A. Hawkes, A.C. Köberle, M. Tavoni, An inter-model assessment of the role of direct air capture in deep mitigation pathways, Nat. Commun. 10 (1) (2019) 3277.
[4] J. Wu, X. Zhu, Y. Chen, R. Wang, T. Ge, The analysis and evaluation of direct air capture adsorbents on the material characterization level, Chem. Eng. J. 450 (2022), 137958.
[5] R.T. Porter, M. Fairweather, C. Kolster, N. Mac Dowell, N. Shah, R.M. Woolley, Cost and performance of some carbon capture technology options for producing different quality CO2 product streams, Int. J. Greenhouse Gas Control 57 (2017) 185–195.
[6] D. Fu, M.E. Davis, Carbon dioxide capture with zeotype materials, Chem. Soc, Rev, 2022.
[7] B. Ray, S.R. Churipard, S.C. Peter, An overview of the materials and methodologies for CO 2 capture under humid conditions, J. Mater. Chem. A 9 (47) (2021) 26498–26527.
[8] R.P. Wijesiri, G.P. Knowles, H. Yeasmin, A.F. Hoadley, A.L. Chaffee, CO2 capture from air using pelletized polyethylenimine impregnated MCF silica, Ind. Eng. Chem. Res. 58 (8) (2019) 3293–3303.
[9] D.G. Madden, H.S. Scott, A. Kumar, K.-J. Chen, R. Sanii, A. Bajpai, M. Lusi, T. Curtin, J.J. Perry, M.J. Zaworotko, Flue-gas and direct-air capture of CO2 by porous metal–organic materials, Philos. Trans. R. Soc. A Math. Phys. Eng. Sci. 375 (2084) (2017) 20160025.
[10] S.M. Wilson, F.H. Tezel, Direct dry air capture of CO2 using VTSA with faujasite zeolites, Ind. Eng. Chem. Res. 59 (18) (2020) 8783–8794.
[11] M. Song, G. Rim, F. Kong, P. Priyadarshini, C. Rosu, R.P. Lively, C.W. Jones, Cold-temperature capture of carbon dioxide with water coproduction from air using commercial zeolites, Ind. Eng. Chem. Res. 61 (36) (2022) 13624–13634.
[12] C. Graves, S.D. Ebbesen, M. Mogensen, K.S. Lackner, Sustainable hydrocarbon fuels by recycling CO2 and H2O with renewable or nuclear energy, Renewable Sustainable Energy Rev. 15 (1) (2011) 1–23.
[13] T. Ji, H. Zhai, C. Wang, C.M. Marin, W.C. Wilfong, Q. Wang, Y. Duan, R. Xia, F. Jiao, Y. Soong, Energy-efficient and water-saving sorbent regeneration at near room temperature for direct air capture, Mater. Today Sustainability 100321 (2023).
[14] X. Xu, H. Asakura, S. Hosokawa, T. Tanaka, K. Teramura, Tuning Ag-modified NaTaO3 to achieve high CO selectivity for the photocatalytic conversion of CO2 using H2O as the electron donor, Appl. Catal., B 320 (2023), 121885.
[15] X. Xu, T. Tanaka, K. Teramura, High selectivity toward CO evolution for the photocatalytic conversion of CO2 by H2O as an electron donor over Ag-loaded β-Ga2O3, Appl. Catal., B 321 (2023), 122027.
[16] Y. Zheng, L. Zhang, J. Guan, S. Qian, Z. Zhang, C.K. Ngaw, S. Wan, S. Wang, J. Lin, Y. Wang, Controlled synthesis of Cu0/Cu2O for efficient photothermal catalytic conversion of CO2 and H2O, ACS Sustainable Chem. Eng. 9 (4) (2021) 1754–1761.
[17] F. Sabatino, A. Grimm, F. Gallucci, M. van Sint Annaland, G.J. Kramer, M. Gazzani, A comparative energy and costs assessment and optimization for direct air capture technologies, Joule 5 (8) (2021) 2047–2076.
[18] L. Jiang, W. Liu, R. Wang, A. Gonzalez-Diaz, M. Rojas-Michaga, S. Michailos, M. Pourkashanian, X. Zhang, C. Font-Palma, Sorption direct air capture with CO2 utilization, Prog. Energy Combust. Sci. 95 (2023), 101069.
[19] K.S. Lackner, The thermodynamics of direct air capture of carbon dioxide, Energy 50 (2013) 38–46.
[20] A. Kumar, D.G. Madden, M. Lusi, K.J. Chen, E.A. Daniels, T. Curtin, J.J. Perry IV, M.J. Zaworotko, Direct air capture of CO2 by physisorbent materials, Angew. Chem. Int. Ed. 54 (48) (2015) 14372–14377.
[21] Y. Deng, J. Li, Y. Miao, D. Izikowitz, A comparative review of performance of nanomaterials for direct air capture, Energy Rep. 7 (2021) 3506–3516.
[22] Y. Wang, R.T. Yang, Chemical liquid deposition modified 4A zeolite as a size-selective adsorbent for methane upgrading, CO2 capture and air separation, ACS Sustainable Chem. Eng. 7 (3) (2019) 3301–3308.
[23] H. Jedli, M. Almoneef, M. Mbarek, A. Jbara, K. Slimi, Adsorption of CO2 onto zeolite ZSM-5: Kinetic, equilibrium and thermodynamic studies, Fuel 321 (2022), 124097.
[24] J. Yu, L.-H. Xie, J.-R. Li, Y. Ma, J.M. Seminario, P.B. Balbuena, CO2 capture and separations using MOFs: computational and experimental studies, Chem. Rev. 117 (14) (2017) 9674–9754.
[25] S. Fujikawa, R. Selyanchyn, T. Kunitake, A new strategy for membrane-based direct air capture, Polym. J. 53 (1) (2021) 111–119.
[26] Y. Fan, C. Zhang, L. Jiang, X. Zhang, L. Qiu, Exploration on two-stage latent thermal energy storage for heat recovery in cryogenic air separation purification system, Energy 239 (2022), 122111.
[27] P. Zhang, X. Bu, Y. Yang, L. Wang, Technical-economic evaluation of an energy-integrated temperature swing adsorption process for compressed air drying, Comput. Chem. Eng. 157 (2022), 107621.
[28] Q. Ke, T. Sun, X. Wei, Y. Guo, S. Wang, Enhanced trace carbon dioxide capture on heteroatom-substituted rho zeolites under humid conditions, ChemSusChem 10 (21) (2017) 4207–4214.
[29] S. Lin, Y. Wei, Z. Liu, Autocatalytic induction period in zeolite-catalyzed methanol conversion, Chem Catal. 3 (5) (2023).
[30] R. Custelcean, N.J. Williams, X. Wang, K.A. Garrabrant, H.J. Martin, M.K. Kidder, A.S. Ivanov, V.S. Bryantsev, Dialing in direct air capture of CO2 by crystal engineering of bisiminoguanidines, ChemSusChem 13 (23) (2020) 6381–6390.
[31] R. Custelcean, Direct air capture of CO 2 via crystal engineering, Chem. Sci. 12 (38) (2021) 12518–12528.
[32] H. Guk, D. Kim, H. Lee, Y.N. Choi, S.Y. Kang, S.-H. Choi, D.H. Chung, Temperature dependence of volume change of nax and nay zeolites using molecular dynamics simulations, J. Phys. Chem. C 118 (24) (2014) 12811–12816.
[33] P. Krokidas, E. Skouras, V. Nikolakis, V. Burganos, Lattice dynamics simulation of thermal contraction of faujasites, J. Phys. Chem. C 114 (51) (2010) 22441–22448.

[34] Q. Zheng, Y. Zhang, M. Montazerian, O. Gulbiten, J.C. Mauro, E.D. Zanotto, Y. Yue, Understanding glass through differential scanning calorimetry, Chem. Rev. 119 (13) (2019) 7848–7939.
[35] J. Drzeżdżon, D. Jacewicz, A. Sielicka, L. Chmurzyński, Characterization of polymers based on differential scanning calorimetry based techniques, TrAC Trends Anal. Chem. 110 (2019) 51–56.
[36] Z.-S. Liu, Y.-H. Peng, C.-Y. Huang, M.-J. Hung, Application of thermogravimetry and differential scanning calorimetry for the evaluation of CO2 adsorption on chemically modified adsorbents, Thermochim Acta 602 (2015) 8–14.
[37] J. Murday, R. Patterson, H. Resing, J. Thompson, N. Turner, Kinetics of surface reactions from nuclear magnetic resonance relaxation times. II. Reaction of water with surface complex in zeolite 13-X, J. Phys. Chem. 79 (24) (1975) 2674–2687.
[38] L. Joos, J.A. Swisher, B. Smit, Molecular simulation study of the competitive adsorption of H2O and CO2 in zeolite 13X, Langmuir 29 (51) (2013) 15936–15942.
[39] W. Ma, S. Xie, X.-G. Zhang, F. Sun, J. Kang, Z. Jiang, Q. Zhang, D.-Y. Wu, Y. Wang, Promoting electrocatalytic CO2 reduction to formate via sulfur-boosting water activation on indium surfaces, Nat. Commun. 10 (1) (2019) 892.
[40] J. Song, J. Liu, W. Zhao, Y. Chen, H. Xiao, X. Shi, Y. Liu, X. Chen, Quaternized chitosan/PVA aerogels for reversible CO2 capture from ambient air, Ind. Eng. Chem. Res. 57 (14) (2018) 4941–4948.
[41] G. Cruciani, Zeolites upon heating: factors governing their thermal stability and structural changes, J. Phys. Chem. Solids 67 (9–10) (2006) 1973–1994.
[42] C.W. Purnomo, C. Salim, H. Hinode, Synthesis of pure Na–X and Na–A zeolite from bagasse fly ash, Microporous Mesoporous Mater. 162 (2012) 6–13.
[43] J.F. Haw, Zeolite acid strength and reaction mechanisms in catalysis, PCCP 4 (22) (2002) 5431–5441.
[44] J.H. Jacobs, C.E. Deering, R. Sui, K.L. Lesage, R.A. Marriott, Degradation of desiccants in temperature swing adsorption processes: the temperature dependent degradation of zeolites 4A, 13X and silica gels, Chem. Eng. J. 451 (2023), 139049.
[45] D.L. Bish, J.W. Carey, Thermal behavior of natural zeolites, Rev. Mineral. Geochem. 45 (1) (2001) 403–452.
[46] G.S. Duthade, U.D. Joshi, M.M. Kodape, S.P. Mardikar, S.J. Uke, V. Pnadit, M. N. Lokhande, Synthesis, X-ray diffraction, physical, thermal behavior and chemical studies of Fe/Zn/Cu-NaX zeolite, Mater. Today: Proc. 53 (2022) 15–23.
[47] G. Cametti, A. Scheinost, S. Churakov, Structural modifications and thermal stability of Cd2+-exchanged stellerite, a zeolite with STI framework type, J. Phys. Chem. C 123 (41) (2019) 25236–25245.
[48] A. Abdoulaye, J. Zanchetta, F. Di Renzo, J. Giuntini, J. Vanderschueren, G. Chabanis, Dielectric properties of faujasites: comparison between types X and Y during dehydration, Microporous Mesoporous Mater. 34 (3) (2000) 317–325.
[49] D. Fu, Y. Park, M.E. Davis, Confinement effects facilitate low-concentration carbon dioxide capture with zeolites, Proc. Natl. Acad. Sci. 119 (39) (2022), e2211544119.
[50] X. Guo, L. Wu, A. Navrotsky, Thermodynamic evidence of flexibility in H 2 O and CO 2 absorption of transition metal ion exchanged zeolite LTA, PCCP 20 (6) (2018) 3970–3978.
[51] N. Öztürk, F. Ucun, A.D. Muhtar, S. Bahçeli, Infrared and SEM analyses of polyethyleneglycol-400 adsorbed on zeolites NaA, CaA, NaX and NaY, *J. Mol. Struct.* 922 (1–3) (2009) 35–38.
[52] S.U. Rege, R.T. Yang, A novel FTIR method for studying mixed gas adsorption at low concentrations: H2O and CO2 on NaX zeolite and γ-alumina, Chem. Eng. Sci. 56 (12) (2001) 3781–3796.
[53] A. Aspelund, Gas purification, compression and liquefaction processes and technology for carbon dioxide (CO2) transport, in: Developments and Innovation in Carbon Dioxide (CO2) Capture and Storage Technology, 2010, pp. 383–407.
[54] M. Shen, L. Tong, S. Yin, C. Liu, L. Wang, W. Feng, Y. Ding, Cryogenic technology progress for CO2 capture under carbon neutrality goals: a review, Sep. Purif. Technol. (2022), 121734.
[55] H. Xi, M. Zhu, K.Y. Lee, X. Wu, Multi-timescale and control-perceptive scheduling approach for flexible operation of power plant-carbon capture system, Fuel 331 (2023), 125695.
[56] P. Zhang, J. Liang, Y. Yang, L. Wang, A new heating system for the air pre-purification of air separation units, Appl. Therm. Eng. 226 (2023), 120194.
[57] L. Tong, P. Zhang, S. Yin, P. Zhang, C. Liu, N. Li, L. Wang, Waste heat recovery method for the air pre-purification system of an air separation unit, Appl. Therm. Eng. 143 (2018) 123–129.
[58] Y. Yang, Y. Chen, Z. Xu, L. Wang, P. Zhang, A three-bed six-step TSA cycle with heat carrier gas recycling and its model-based performance assessment for gas drying, Sep. Purif. Technol. 237 (2020), 116335.
[59] T. Carey, C.C. Tang, J.A. Hriljac, P.A. Anderson, Chemical control of thermal expansion in cation-exchanged zeolite A, Chem. Mater. 26 (4) (2014) 1561–1566.
[60] W. Jeong, J. Kim, Understanding the mechanisms of CO2 adsorption enhancement in pure silica zeolites under humid conditions, J. Phys. Chem. C 120 (41) (2016) 23500–23510.

Impact of H_2O on CO_2 Adsorption and Co-Adsorption: Mechanism and High-Performance Adsorbents for Efficient H_2O-CO_2 Capture

Minghai Shen[1,2], Fulin Kong[1,2], Wei Guo[1,2], Zhongqi Zuo[1,2], Ting Gao[1,3], Sen Chen[4], Lige Tong[1,2]*, Peikun Zhang[1,2], Li Wang[1,2], Paul K. Chu[5]*, Yulong Ding[6]*

[1] School of Energy and Environmental Engineering, University of Science and Technology Beijing, Beijing 100083, China

[2] Beijing Key Laboratory of Energy Saving and Emission Reduction for Metallurgical Industry, University of Science and Technology Beijing, Beijing 100083, China

[3] Experimental Center, School of Energy and Environmental Engineering, University of Science and Technology Beijing, Beijing 100083, China

[4] Basic Experimental Center of Natural Science, University of Science and Technology Beijing, Beijing 100083, China

[5] Department of Physics, Department of Materials Science and Engineering, and Department of Biomedical Engineering, City University of Hong Kong, Tat Chee Avenue, Kowloon, Hong Kong, China

[6] Birmingham Centre for Energy Storage & School of Chemical Engineering, University of Birmingham, B15 2TT, UK

Corresponding authors: Lige Tong (tonglige@me.ustb.edu.cn); Paul K. Chu

(paul.chu@cityu.edu.hk); Yulong Ding (Y.Ding@bham.ac.uk);

Table of Contents

Table S1. Characteristics of commercial NaX zeolites.

Figure S1. SEM image of the commercial NaX zeolite tested in the experiment.

Figure S2. XRD spectra of commercial NaX zeolites used in the experiment.

Figure S3. Effects of temperature on the porous structure of commercial NaX zeolites and direct air carbon capture based on thermogravimetric and desorption analyses.

Figure S4. Transverse relaxation time of H_2O adsorption on NaX at different temperatures.

Table S2. Adsorption binding energy between molecules.

Figure S5. MS simulation of the respective and common adsorption properties of CO_2 and H_2O in NaX at low partial pressure: (a) and (b) Adsorption curves of CO_2 and H_2O; (c) Diffusion rates of CO_2 and H_2O adsorption and co-adsorption; (e) Energy distributions of CO_2 and H_2O adsorption.

Table S3. Faujasites lattice parameters of NaX obtained by MD simulations.

Table S4. Variation in bond lengths and bond angles of NaX zeolites at different treatment temperatures simulated by MS.

Figure S6. Molecular dynamics simulation of the NaX skeleton changes at different treatment temperatures: (a) and (b) Vibrational contraction of Si_1-Si_1, Al_1-Al_1; (c and d) Angle change of O-T-O (T=Al,Si).

Table S5. Trajectories of Na_3 at different treatment temperatures simulated by MS.

Figure S7. TG-DSC curves of NaX zeolite at 50-500 ℃.

Figure S8. Structure of NaX zeolite treated at different temperatures.

Figure S9. XRD patterns of NaX zeolite treated at different temperatures.

Table S6. Temperature effects on the specific surface area, pore volume, and pore size of NaX zeolite.

Figure S10. Skeleton change of NaX at different temperatures: (a) XPS survey spectra of NaX and (b) XPS Na 1*s* spectra.

Figure S11. Desorption heat flow of CO_2 and H_2O in NaX at different temperatures.

Figure S12. Fitted peaks of desorption heat flow of CO_2 and H_2O in NaX at different treatment temperatures.

Figure S13. MS simulation of the respective and common adsorption properties of CO_2 and H_2O in NaX at low partial pressure: (a) Adsorption curves when CO_2 and H_2O adsorb together; (b) Energy distributions during co-adsorption of CO_2 and H_2O.

Figure S14. Energy distributions for co-adsorption of CO_2 and H_2O by NaX at different temperatures simulated by MS.

Figure S15. EDS elements of samples treated at different temperatures.

Figure S16. Flow diagram of H_2O and CO_2 condensation recovery system suggested based on Aspen Plus software.

Table S7. Energy consumption of condensation dehydration for different compositions of CO_2 and H_2O.

References

Table S1. Characteristics of commercial NaX zeolites.

Indicators	Units	Parameters
Diameter	mm	1.6-2.5
Hydrostatic adsorption	%wt	≥26.5（RH75%,25℃）
Static CO_2 adsorption	%wt	≥18.5 （25℃,250mmHg）
Stacking density	g/ml	≥0.64（Vibranium）
Crush resistance	N	≥30（Average）
Abrasion rate	%wt	≤0.1
Relative standard deviation of crush resistance	-	≤0.3
Grain size	%	≥98
Water content of packaged products	%wt	≤1.5（575℃，1h）

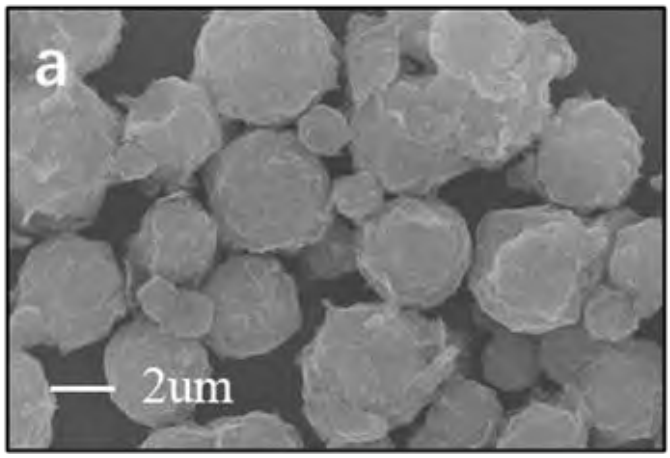

Figure S1. SEM image of the commercial NaX zeolite tested in the experiment.

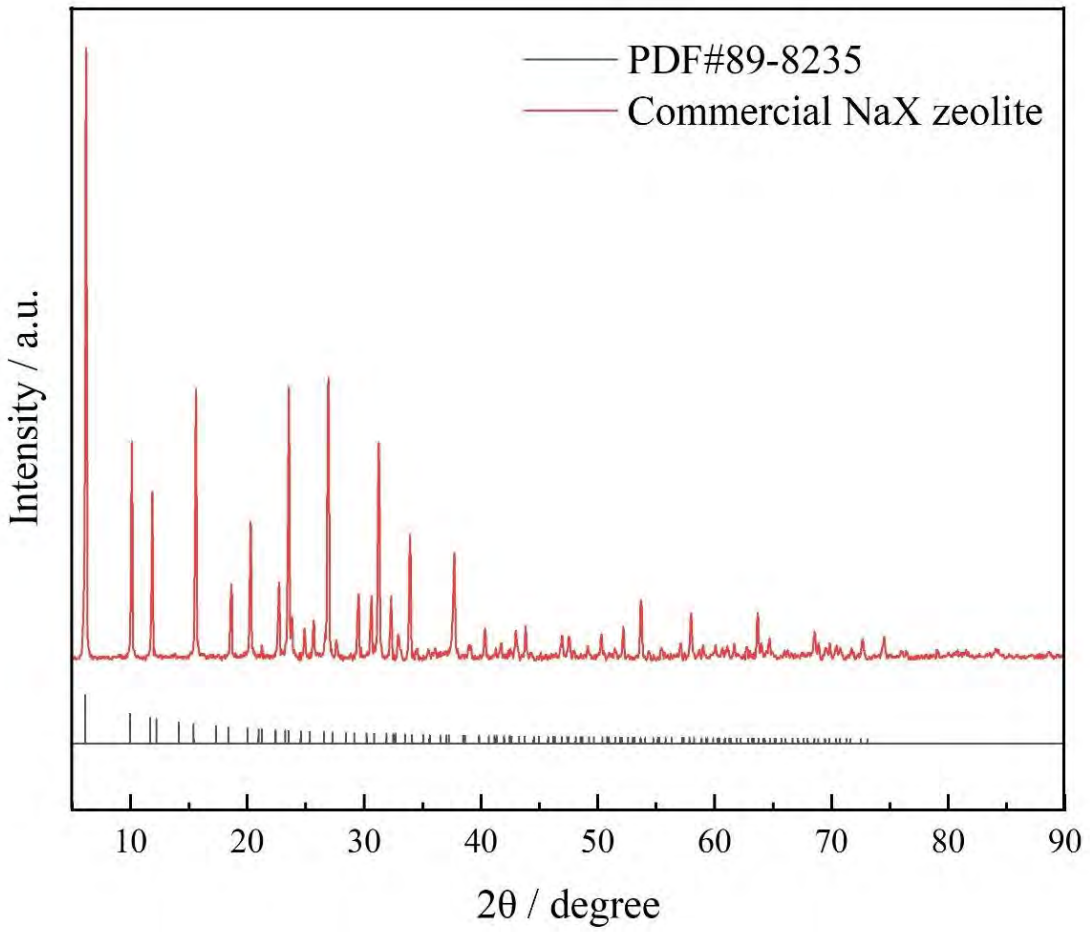

Figure S2. XRD spectra of commercial NaX zeolites used in the experiment.

Except for a few miscellaneous peaks, the pattern is basically consistent with the XRD pattern of the standard Zeolite X (dehydrated) [1]. The few impurity peaks may be due to the addition of a certain amount of adhesive (kaolin) to the commercial zeolite molecular sieves during synthesis [2]. The adhesive is used to produce a certain shape (spherical, bar, etc.) for the zeolite molecular sieve, so that it can be better applied to industrial production. Figure S1 also verifies this phenomenon.

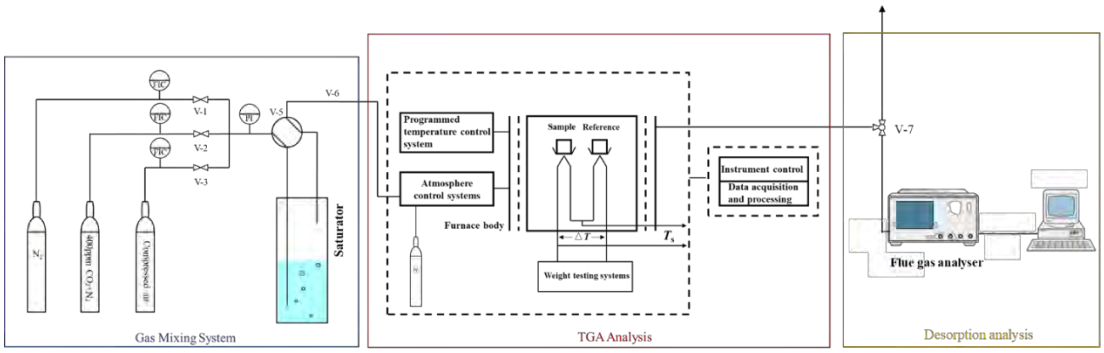

Figure S3. Effects of temperature on the porous structure of commercial NaX zeolites and direct air carbon capture based on thermogravimetric and desorption analyses.

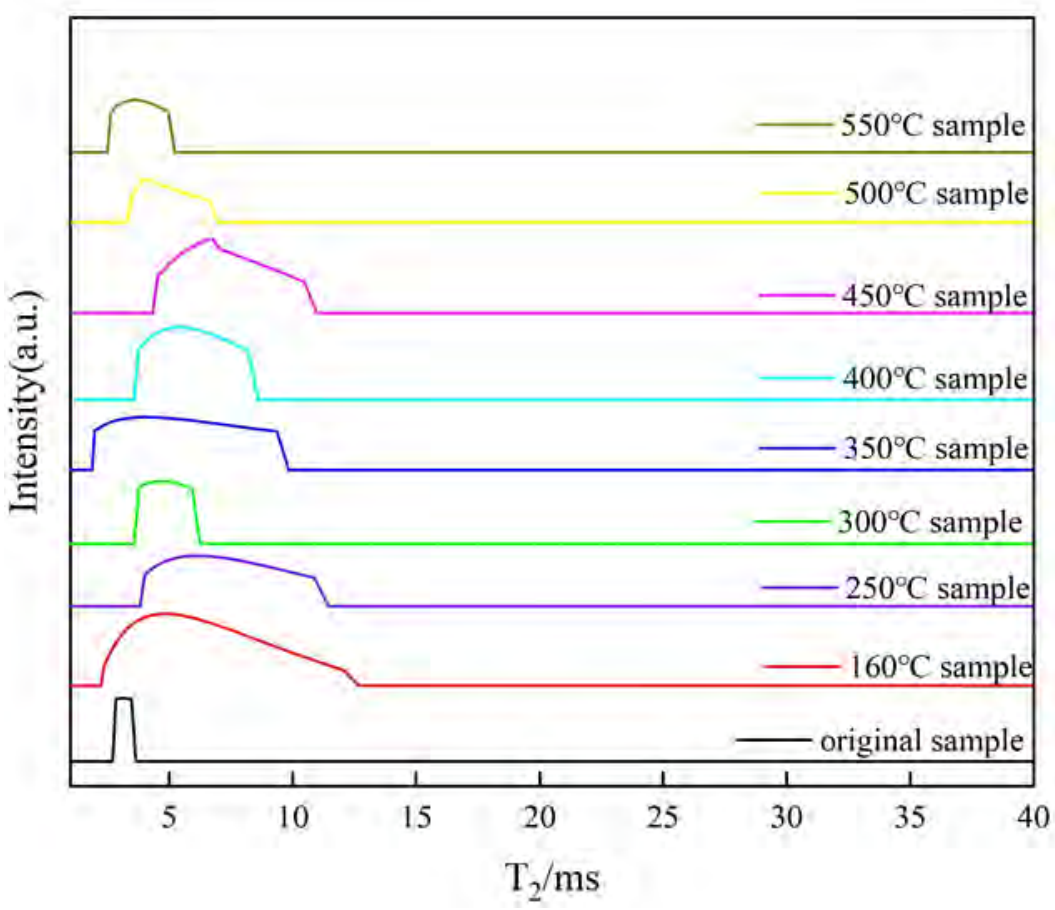

Figure S4. Transverse relaxation time of H_2O adsorption on NaX at different temperatures.

Table S2. Adsorption binding energy between molecules.

Adsorbed molecules	E_{A-B}	E_A	E_B	Ha	Binding energy (kcal/mol)
CO_2-H_2O	-264.8657	-188.4797	-76.3827	-0.003352	-2.1034
H_2O-H_2O	-152.7745	-76.3827	-76.3827	-0.009112	-5.7179
CO_2-CO_2	-376.9591	-188.4797	-188.4797	0.000219	0.1374

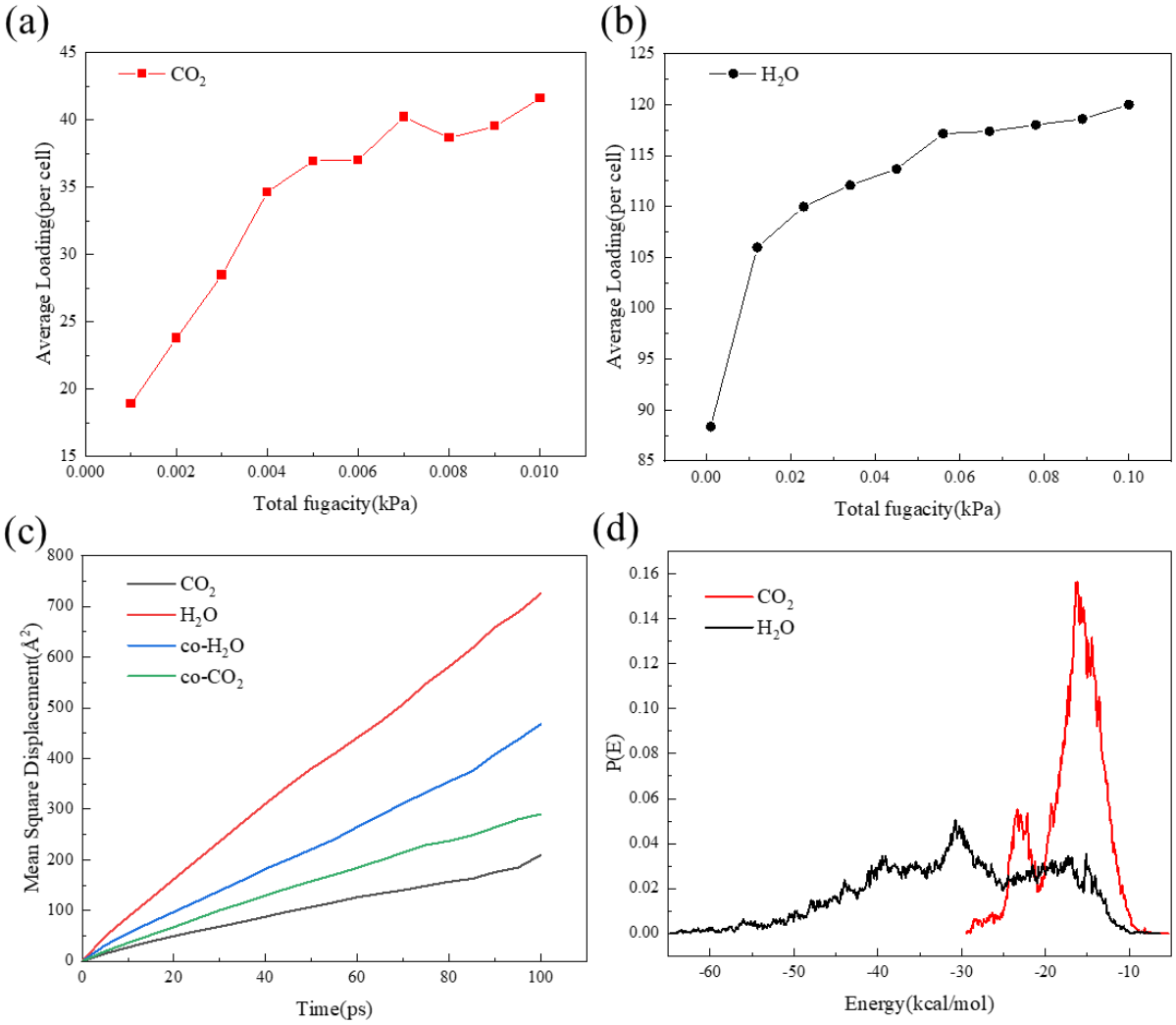

Figure S5. MS simulation of the respective and common adsorption properties of CO_2 and H_2O in NaX at low partial pressure: (a) and (b) Adsorption curves of CO_2 and H_2O; (c) Diffusion rates of CO_2 and H_2O adsorption and co-adsorption; (e) Energy distributions of CO_2 and H_2O adsorption.

Table S3. Faujasites lattice parameters of NaX obtained by MD simulations.

Temperature	a (Å)	b (Å)	c (Å)	α (°)	β (°)	γ (°)
50	25.43	25.4	25.41	89.59	90.08	89.77
100	25.42	25.41	25.4	90.01	90.07	90
200	25.55	25.43	25.45	90.31	89.97	89.79
300	25.42	25.53	25.48	90.13	90.51	90.14
433.15(160℃)	25.54	25.53	25.44	90.08	90.13	90.3
523.15(250℃)	25.5	25.63	25.58	90.04	90.04	89.67
573.15(300℃)	25.6	25.51	25.61	89.99	89.79	89.99
623.15(350℃)	25.62	25.62	25.51	89.99	89.87	90.18
673.15(400℃)	25.75	25.79	25.4	90.07	90.34	90.14
723.15(450℃)	25.52	25.72	25.61	90.4	90.66	89.86
773.15(500℃)	25.58	25.66	25.69	90.23	90.2	89.92
823.15(550℃)	25.66	25.65	25.65	90.06	89.82	90.42

Table S4. Variation in bond lengths and bond angles of NaX zeolites at different treatment temperatures simulated by MS.

Temperature	Bond lengths(Å)		Bond angles(°)	
(K)	Si_1-Si_1	Al_1-Al_1	O_3-Al_1-O_1	O_1-Si_1-O_3
50	11.9276	11.9909	116.879	116.748
100	11.9303	11.9694	115.76	112.855
200	12.0911	11.9856	115.591	118.946
300	12.0242	12.1258	115.632	118.315
433.15(160℃)	11.9697	12.0667	113.97	117.731
523.15(250℃)	12.353	12.1118	112.416	108.993
573.15(300℃)	11.9904	12.3339	114.214	109.732
623.15(350℃)	11.8491	12.0462	116.155	112.141
673.15(400℃)	12.0849	12.1607	115.024	117.274
723.15(450℃)	12.2578	12.6625	115.22	117.187
773.15(500℃)	12.1015	12.0699	115.478	117.781
823.15(550℃)	12.1122	12.0047	125.33	117.228

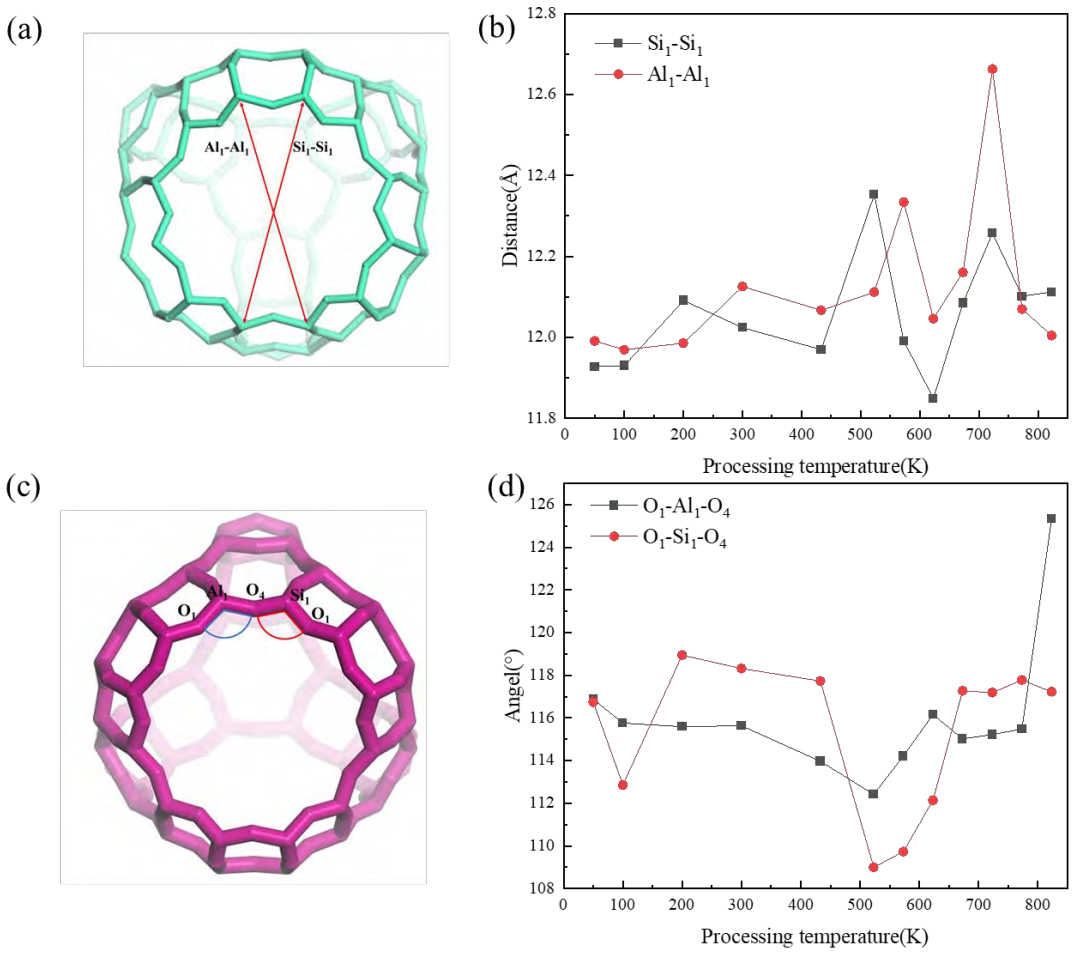

Figure S6. Molecular dynamics simulation of the NaX skeleton changes at different treatment temperatures: (a) and (b) Vibrational contraction of Si_1-Si_1, Al_1-Al_1; (c and d) Angle change of O-T-O (T=Al,Si).

Table S5. Trajectories of Na_3 at different treatment temperatures simulated by MS.

Temperature (K)	Na_3 distances (Å)			Na_3 angles (°)
	Na_3-Al_1	Na_3-O_4	Na_3-Si_1	O_2-O_4-Na_3
50	6.51356	5.85458	6.3838	103.937
100	7.65226	7.18167	7.76189	72.6198
200	2.98184	2.28742	3.27878	71.0187
300	5.13138	3.85946	3.49435	135.46
433.15(160℃)	9.18042	8.35652	8.77909	116.925
523.15(250℃)	8.54514	7.37616	7.54863	111.804
573.15(300℃)	5.5197	4.117	3.88898	117.227
623.15(350℃)	7.42645	7.29895	8.42407	113.592
673.15(400℃)	3.83736	2.33588	2.54254	114.166
723.15(450℃)	3.91877	4.1572	5.05845	135.856
773.15(500℃)	4.98554	3.81373	3.51423	137.11
823.15(550℃)	3.51953	4.17194	5.60679	99.5527

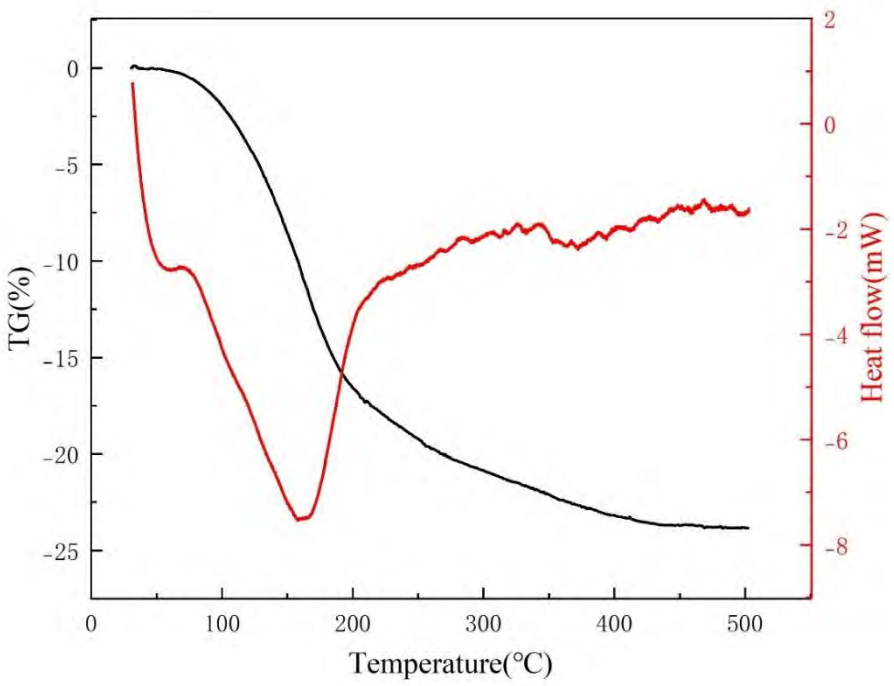

Figure S7. TG-DSC curves of NaX zeolite at 50-500 ℃.

The main weight loss of NaX zeolite at 50-500 ℃ is caused by adsorbed water and crystal water (crystal frame surface and between crystal frames). As the temperature goes up due to evaporation, the weight loss ratio is 23.8wt%. There is only one heat absorption peak suggesting only water heat absorption.

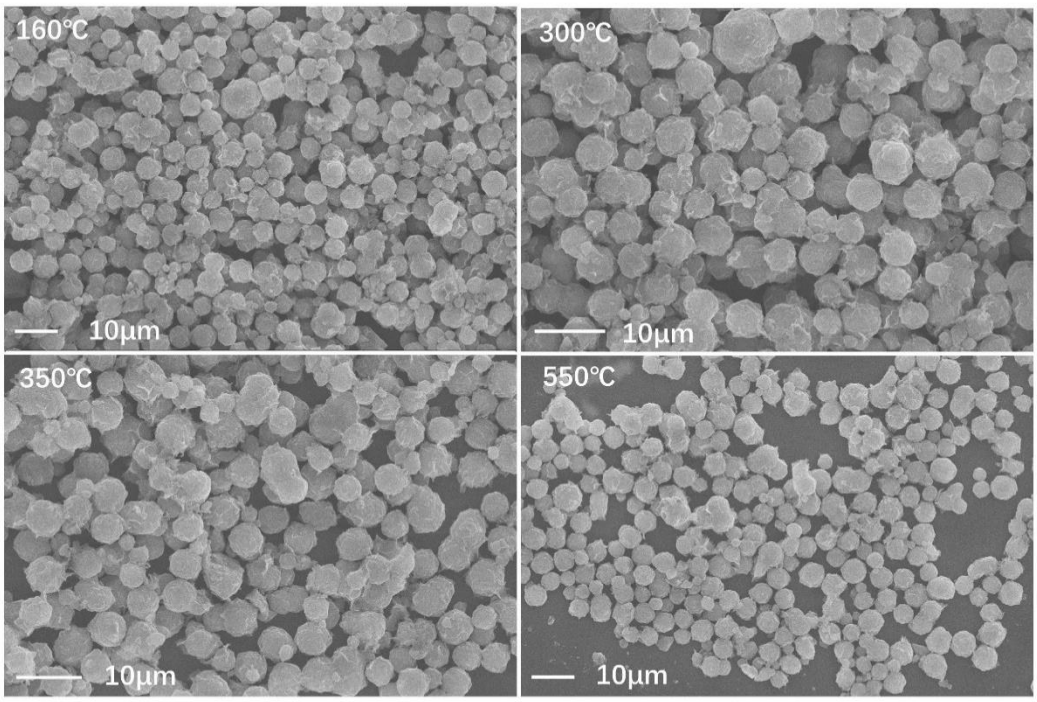

Figure S8. Structure of NaX zeolite treated at different temperatures.

According to the SEM images, commercial 13X is treated at 160 ℃ (pre-dehydration) and 300-550 ℃. The morphology and size of the particles do not change significantly and the structure is stable [3].

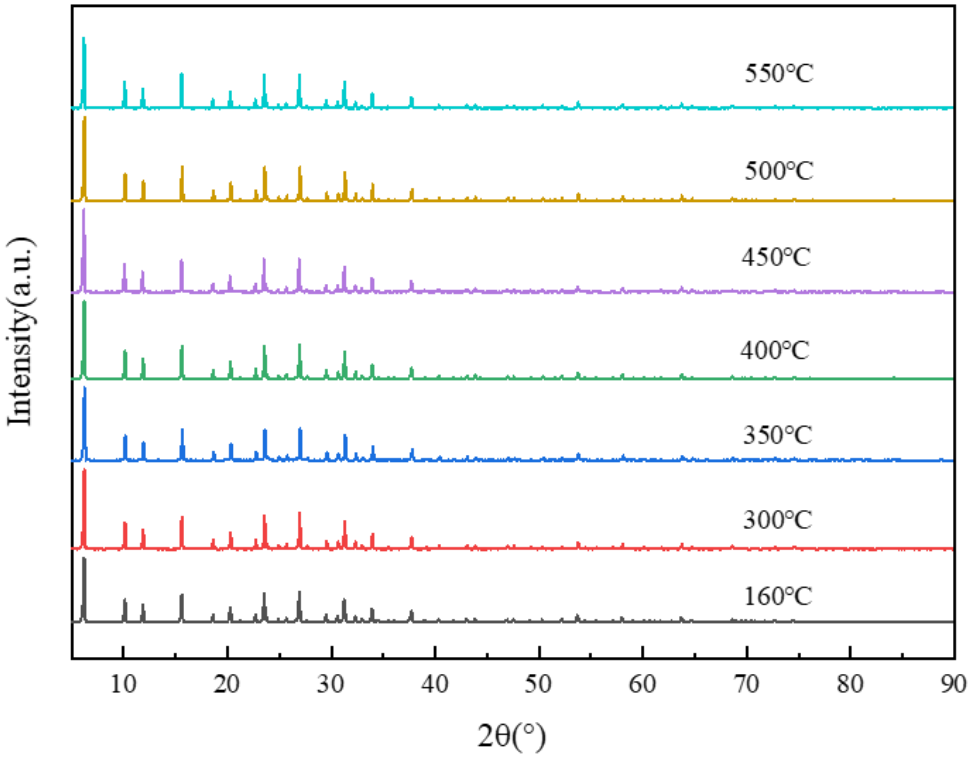

Figure S9. XRD patterns of NaX zeolite treated at different temperatures.

Table S6. Temperature effects on the specific surface area, pore volume, and pore size of NaX zeolite.

Parameters		Original sample	300℃ sample	350℃ sample	550℃ sample
Specific surface area	Single point method for specific surface area (m^2/g)	593.0174	558.3383	556.8425	544.2700
	BET Surface Area (m^2/g)	596.2447	559.7259	558.1265	545.9120
Pore volume	Single point method pore capacity (cm^3/g)	0.325997	0.307209	0.310125	0.311640
Pore size	Adsorption average pore diameter (4V/A by BET)（nm）	2.1870	2.1954	2.2226	2.2834

BJH Adsorption average pore width (4V/A) (nm)	8.9558	9.2854	9.1403	8.1540

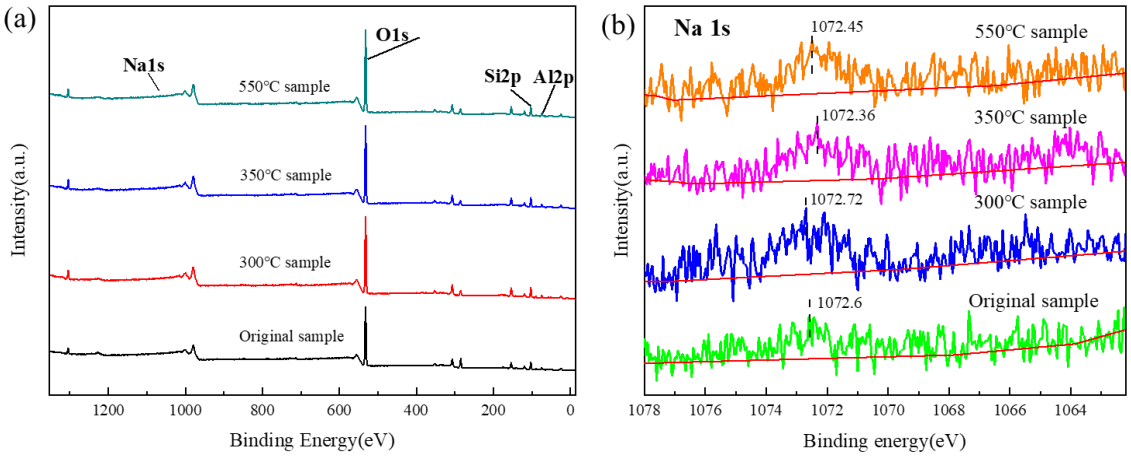

Figure S10. Skeleton change of NaX at different temperatures: (a) XPS survey spectra of NaX and (b) XPS Na 1*s* spectra.

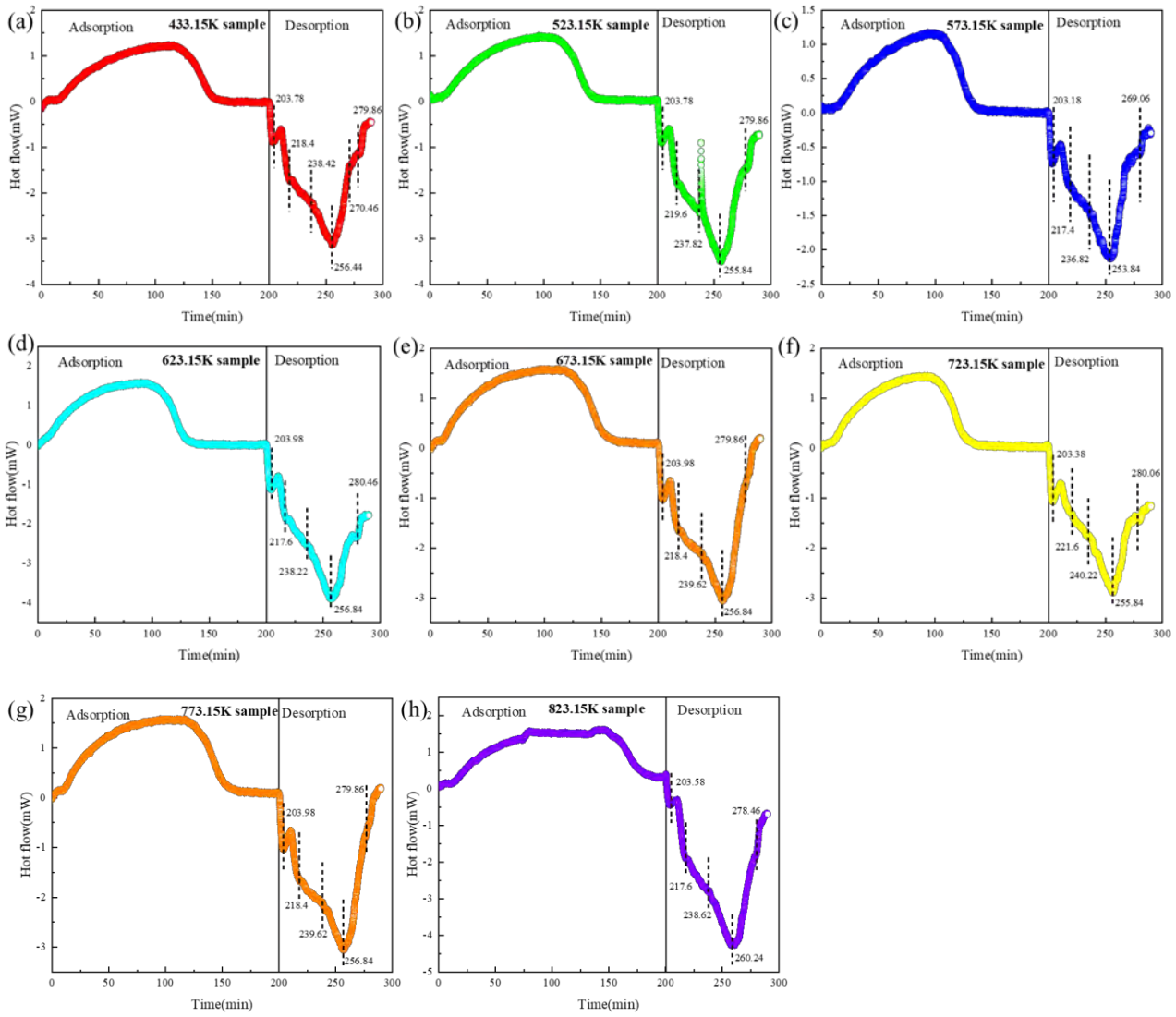

Figure S11. Desorption heat flow of CO_2 and H_2O in NaX at different temperatures.

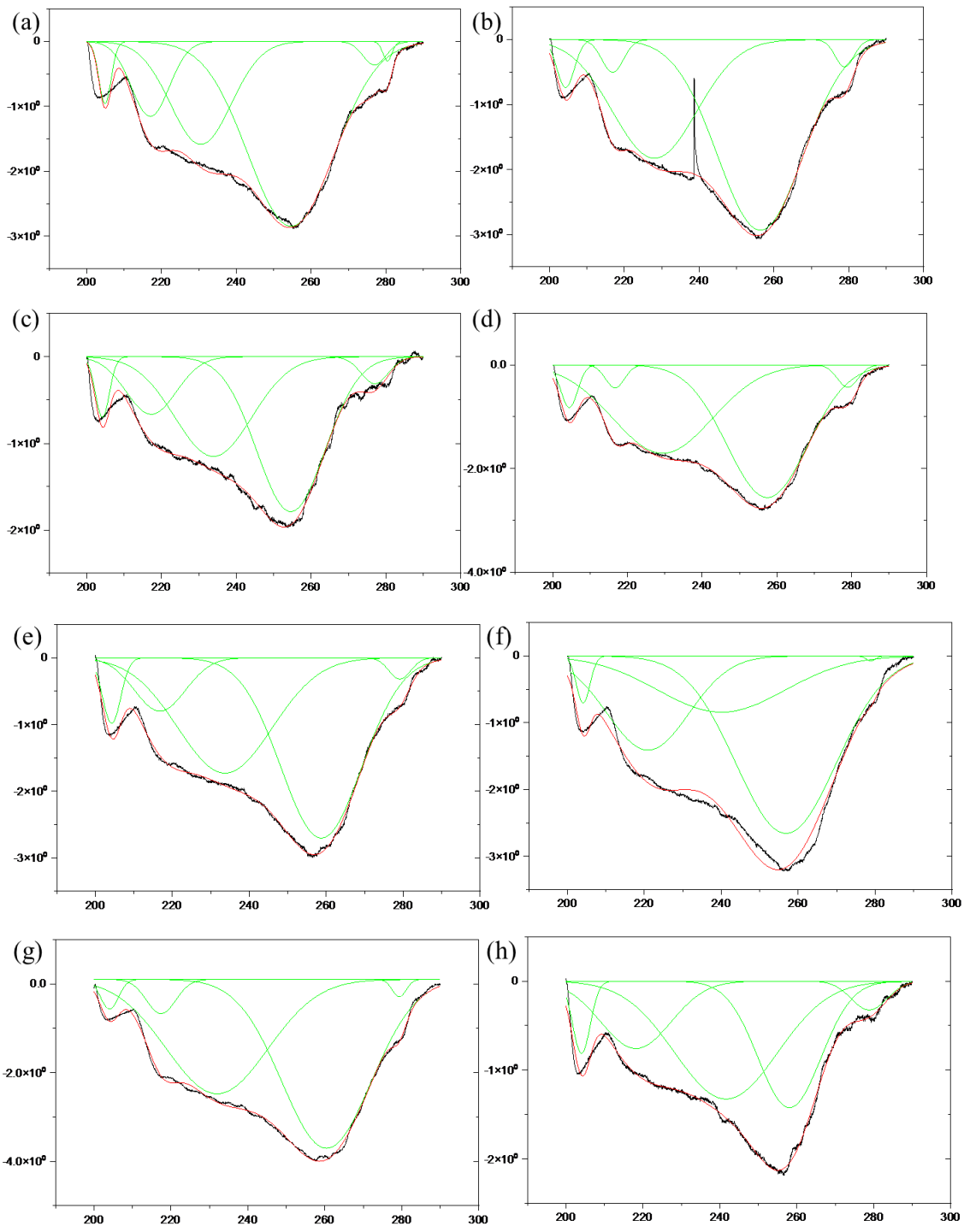

Figure S12. Fitted peaks of desorption heat flow of CO_2 and H_2O in NaX at different treatment temperatures.

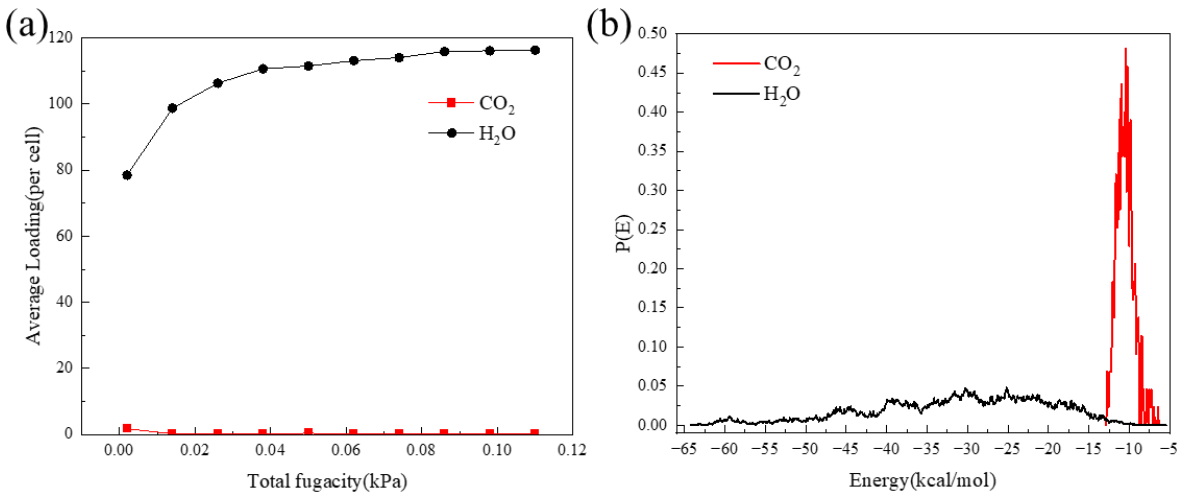

Figure S13. MS simulation of the respective and common adsorption properties of CO_2 and H_2O in NaX at low partial pressure: (a) Adsorption curves when CO_2 and H_2O adsorb together; (b) Energy distributions during co-adsorption of CO_2 and H_2O.

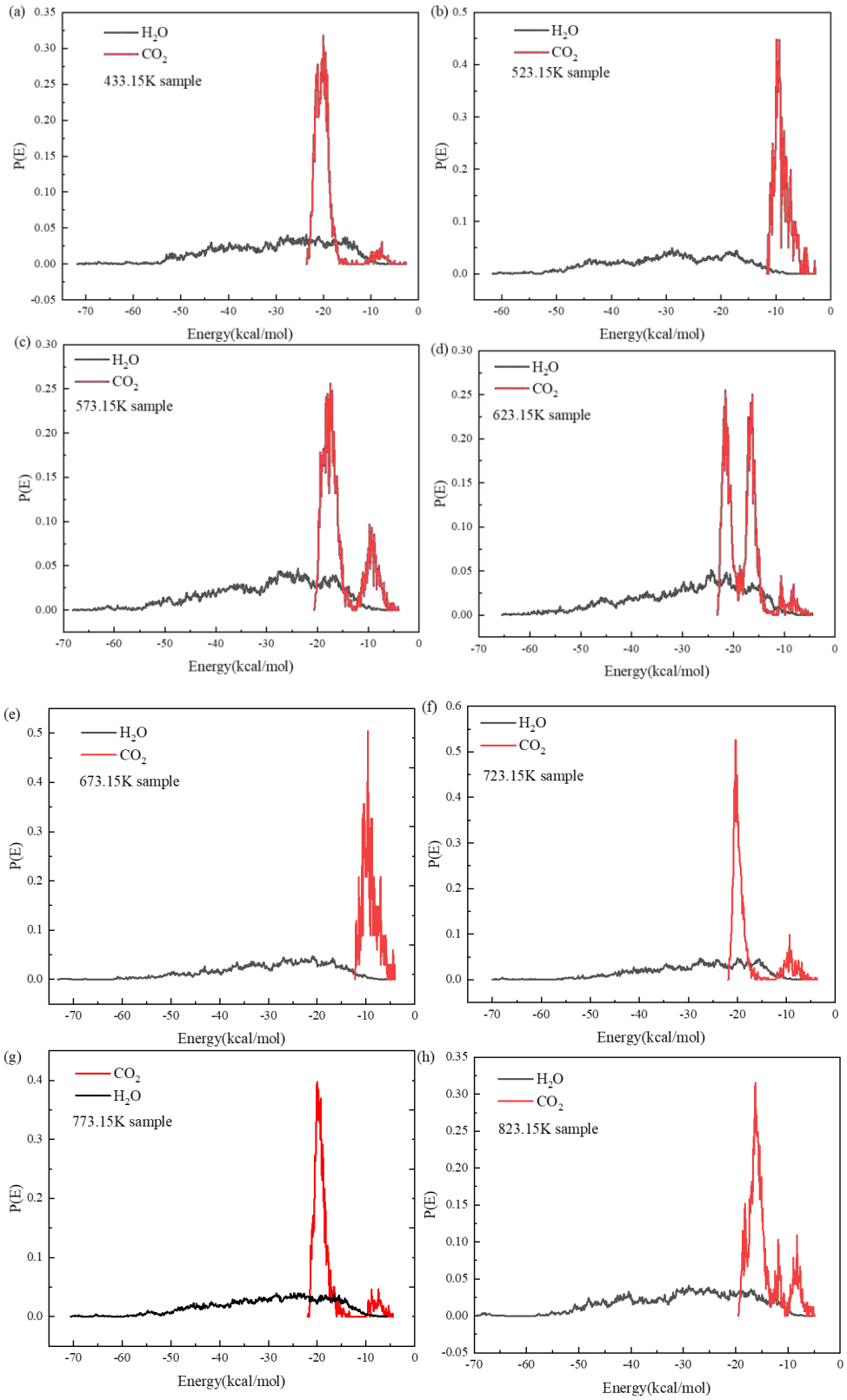

Figure S14. Energy distributions for co-adsorption of CO_2 and H_2O by NaX at different temperatures simulated by MS.

Figure. S14 shows that the structural changes caused by the temperature effects affect the binding energies of adsorption of CO_2 and H_2O. During co-adsorption, there is only one energy peak of CO_2 as shown in Figure S10f, while Figures S14a, c, d, f, g, and h reveal a variety of CO_2 adsorption energy peaks.

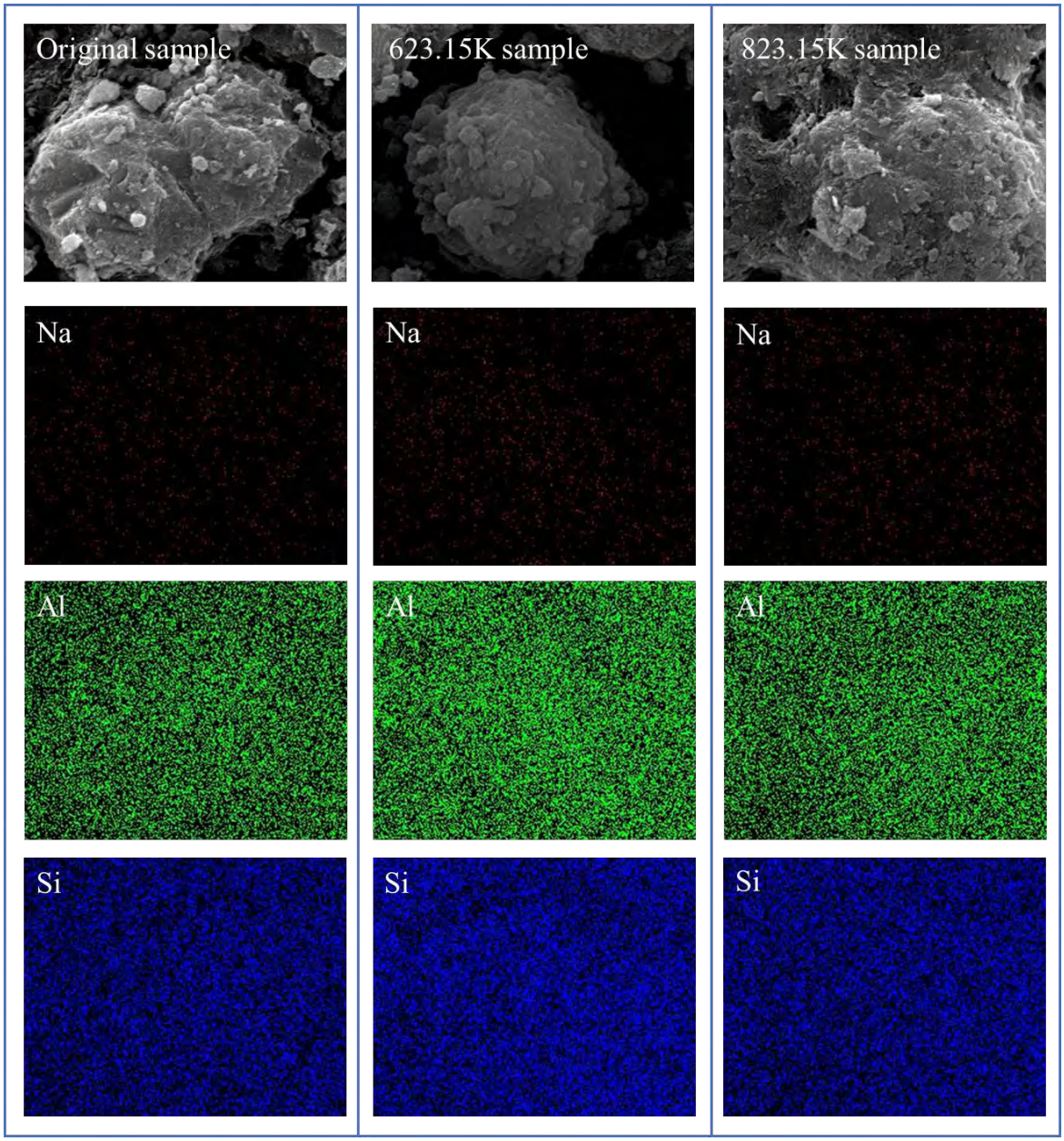

Figure S15. EDS elements of samples treated at different temperatures.

As the contraction vibration of the O-T-O (Al,Si) skeleton is limited as shown in Figure S15, the distribution changes of Al and Si caused by the temperature effect are not obvious. Na acts as a metallic element in the zeolite. Its concentration is relatively small, but the distribution is not uniform. The temperature effect results in migration of Na^+. However, owing to the limitations of the O-T-O (Al,Si) skeleton and steric hindrance, it does not give rise to a significant density or dispersion. The EDS map of Na in Figure S15 reveals regions where Na^+ is not found (regions with a black color).

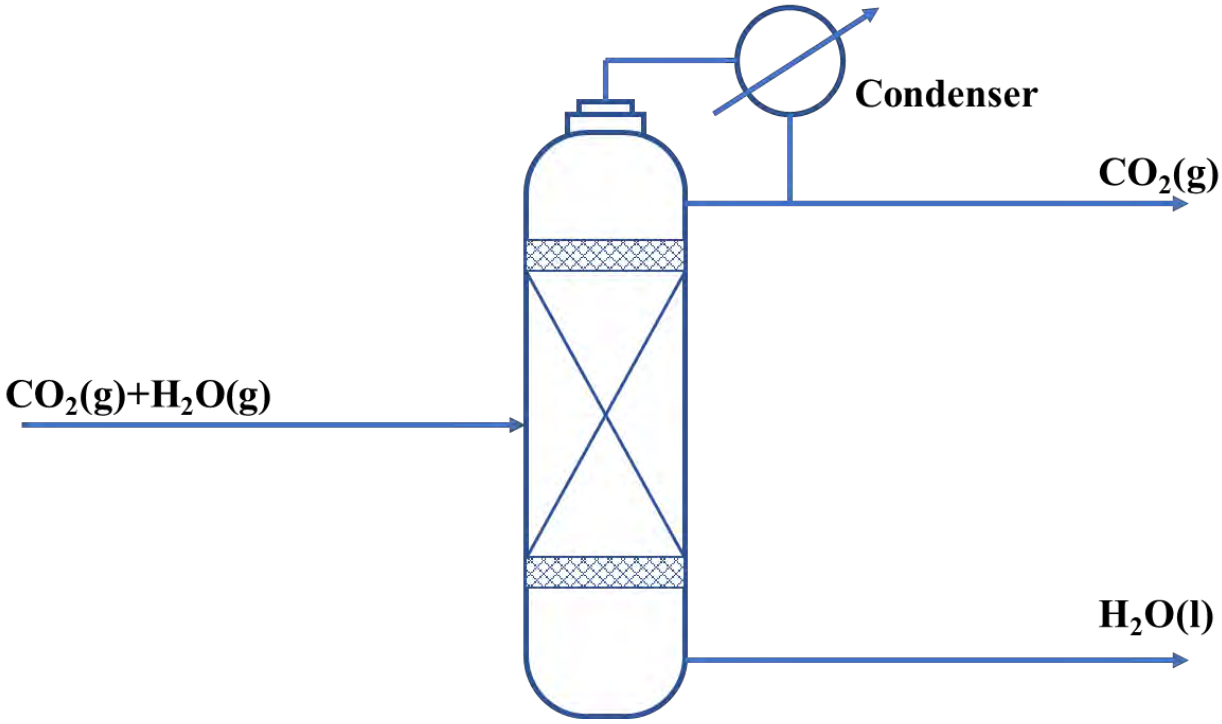

Figure S16. Flow diagram of H_2O and CO_2 condensation recovery system suggested based on Aspen Plus software.

In AspenTech software such as Aspen Plus or Aspen HYSYS, the calculation of water cooling energy consumption is usually based on thermodynamic principles and the heat balance of the system. The calculation of water cooling energy consumption can be achieved through the following steps:

For water coolers, the energy consumption is usually related to the cooling or heating process of water. Water cooler energy consumption (Q) can be calculated by the following formula:

$$Q = m \cdot C_p \cdot \Delta T \quad (1)$$

Among them, m is the mass flow rate of water (kg/s), C_p is the specific heat capacity of water (J/(kg·°C)), and ΔT is the temperature change of water (°C).

This formula describes the energy consumption of cooling or heating water in a water cooler, which absorbs or releases heat by changing the temperature of the water.

This calculation uses industrial circulating cooling water with an inlet temperature of 20°C. The specific heat capacity of water is 4.2×10^3 J/(kg·°C).

The outlet temperature of the circulating water changes with the percentage of H2O recovery set in the condensation unit. The condenser module is automatically calculated in Aspen Plus software.

Table S7. Energy consumption of condensation dehydration for different compositions of CO_2 and H_2O.

Inlet water vapor content (%)	Outlet water vapor content (%)	CO_2 purity (%)	Cold energy (kW)	Recirculating cooling water flow (kg/s)
1	0.01	99.99	-11.92	0.5697
1	0.10	99.90	-10.87	0.5196
5	0.01	99.99	-14.23	0.6802
5	0.10	99.90	-13.13	0.6278
5	1	99	-11.32	0.5411
10	0.01	99.99	-17.11	0.8183
10	0.10	99.90	-15.96	0.7631
10	1	99	-14.1	0.6742
20	0.01	99.99	-22.89	1.095
20	0.10	99.90	-21.62	1.034
20	1	99	-19.67	0.9404
40	0.01	99.99	-34.44	1.647
40	0.10	99.90	-32.93	1.575
40	1	99	-30.8	1.473
60	0.01	99.99	-46	2.199
60	0.10	99.90	-44.25	2.116

60	1	99	-41.94	2.005
80	0.01	99.99	-57.55	2.752
80	0.10	99.90	-55.56	2.657
80	1	99	-53.07	2.538

References

[1] P. Krokidas, E. Skouras, V. Nikolakis, V. Burganos, *The Journal of Physical Chemistry C* **2010**, *114*, 22441-22448.

[2] M. Ansari, A. Aroujalian, A. Raisi, B. Dabir and M. Fathizadeh, *Advanced Powder Technology* **2014**, 25, 722-727.

[3] D. H. Olson, Zeolites, 1995, 15, 439-443.